www.sciencemag.org/content/357/6347/195/suppl/DC1

Supplementary Materials for

Control and local measurement of the spin chemical potential in a magnetic insulator

Chunhui Du, Toeno van der Sar, Tony X. Zhou, Pramey Upadhyaya, Francesco Casola, Huiliang Zhang, Mehmet C. Onbasli, Caroline A. Ross, Ronald L. Walsworth, Yaroslav Tserkovnyak, Amir Yacoby*

*Corresponding author. Email: yacoby@physics.harvard.edu

Published 14 July 2017, *Science* **357**, 195 (2017)
DOI: 10.1126/science.aak9611

This PDF file includes:

Materials and Methods
Supplementary Text
Figs. S1 to S11
References

Materials and Methods

$Y_3Fe_5O_{12}$ (YIG) thin-film growth and YIG-device fabrication

The 20 nm YIG thin film used in this work is grown by Pulsed Laser Deposition (PLD) on a (111)-oriented $Gd_3Ga_5O_{12}$ (GGG) substrate. The growth details were reported in (*28*). The saturation magnetization of the film is $M_s = 1.24 \cdot 10^5$ A/m, determined from fitting the ferromagnetic resonance (FMR) vs field data shown in Fig. 2C of the main text (see Section S4 for details), in agreement with M_s measured by vibrating sample magnetometry. The root mean square (RMS) surface roughness was 0.14 nm and the coercivity of the unpatterned film was below 0.2 mT for an in-plane field. The film has an in-plane easy axis. To yield a narrow FMR linewidth, the sample was annealed in-situ at 750 °C and 500 Torr of oxygen pressure for 10 minutes before breaking the vacuum. After annealing, the film was slowly cooled down (*33*).

We use three photolithography steps to fabricate the Au and Pt striplines onto the YIG film. The first step defines Au alignment markers and the Au stripline, which we deposit by e-beam evaporation of 15 nm/600 nm Ti/Au. In the second step we define the Pt stripline, which we deposit by DC sputtering of 10 nm Pt using an Ar plasma. The last step defines bonding pads, which we deposit using e-beam evaporation of 10 nm/100 nm Ti/Au. All lithography steps were performed using a bi-layer of resist to yield clean liftoffs. Before each metal deposition step, we used O_2 plasma to remove resist residue. The resulting Au and Pt striplines are 7 μm and 3.2 μm wide respectively, and can be seen in Fig. 1D of the main text.

Fabrication and transfer of diamond nanobeams

To ensure a close proximity of the nitrogen-vacancy (NV) centers to the YIG film, we position NV-containing diamond nanobeams directly onto the YIG surface. The nanobeams are fabricated from a diamond grown using chemical vapor deposition (CVD) by the company Apollo (now ScioDiamond). The NV centers used in this work were naturally incorporated during growth at a density of about $1/\mu m^3$.

Following the fabrication procedure described in (*21*), we angle-etch nanobeams into the 100 surface of the diamond with their long axis oriented along the 011 direction. Using a tungsten tip, we first break several nanobeams free from the sample. These nanobeams typically land on the diamond surface. We then use a tungsten tip to pick up an individual nanobeam and transfer it onto the YIG chip. The whole procedure is performed under a long working distance microscope equipped with a micro-manipulator that has sub-micron resolution and is backlash free down to ~50-100 nm.

Measurement setup

We optically address individual NV centers using a home-built scanning confocal microscope setup (Fig. S1). Laser pulses for optical initialization and readout of the NV spin are generated by an acousto-optical modulator (AOM) in double-pass configuration. NV spin states are read out by integrating the photoluminescence (PL) intensity for the first few 300-700 ns of a laser readout pulse.

The microwave (MW) pulses used to control the NV spin states and to excite magnons in the YIG are generated by amplitude modulation of a Rohde & Schwarz SGS100a or a Rohde & Schwarz SMB100a microwave source. The SGS100a allows direct

amplitude modulation via its I/Q inputs. Signals generated by the SMB100a are amplitude modulated using a MW switch (Minicircuits ZASWA-2-50DR+). The pulses for amplitude modulation are generated by an arbitrary waveform generator (Tektronix AWG5014C). The MW signals are amplified by a broadband amplifier (AR 25S1G6) and delivered to the on-chip Au stripline through a printed circuit board.

The external magnetic field B_{ext} is applied using a cylindrical NdFeB permanent magnet (K&J D48N52). To assure good optical spin contrast of the NV center under study, we move the magnet along a trajectory that keeps B_{ext} aligned with the NV axis using the procedure described in the supplement of (*24*). From this trajectory, we determine the orientation of the NV centers under study. We find that the axis of NV_1 makes a $\theta = 65^{\text{o}}$ angle with respect to the sample-plane normal, and a $\phi = 52^{\text{o}}$ in-plane angle with respect to the Au stripline. For NV_2, $\theta = 65^{\text{o}}$ and $\phi = 6^{\text{o}}$. Fig. S2A shows a confocal photoluminescence image of NV_2 and its position with respect to the Au and Pt striplines. A $g^{(2)}$ measurement (Fig. S2B) confirms that we are studying single NV centers (*34*).

Nanometer proximity of the NV centers to the YIG surface is essential to probe the magnetic noise generated by spin fluctuations in the YIG. The NV-sample distances of NV_1 and NV_2 are 109 ± 10 nm and 65 ± 10 nm respectively, obtained from the NV relaxation rate measurements as described in detail in Section S3.

Supplementary Text

Section S1. Calibration of the on-chip amplitude of the AC magnetic field used to excite magnons in the YIG film

A unique advantage of using an NV spin to investigate driven magnon phenomena is the ability to precisely quantify the on-chip amplitude B_{AC} of an AC magnetic drive field. This ability allowed us to perform a quantitative analysis of the increase in chemical potential vs drive power B_{AC}^2 (presented in Fig. 3D of the main text) leading to the determination of the local thermomagnonic torque. In this section we describe the calibration procedure for the on-chip amplitude B_{AC}.

In general, quantifying the on-chip magnetic-field amplitude produced by a MW current flowing through an on-chip stripline or waveguide is challenging: the transmission from MW source to chip typically depends on the MW frequency because of reflections and absorption in MW components such as the cables, connectors, printed circuit board, and bonding wires used in our setup. We characterize the resulting frequency-dependent power delivery to the sample using the following procedure.

The amplitude of an AC magnetic field applied at the NV electron spin resonance (ESR) frequency can be precisely quantified by measuring the NV spin rotation rate (Rabi frequency) f_{R}. The Rabi frequency is given by $f_{\text{R}} = \frac{\gamma B_{\text{AC}\perp}}{2\pi\sqrt{2}}$, where $B_{\text{AC}\perp}$ is the component of the drive field perpendicular to the NV axis (Fig. S3A) (see supplement of (*35*)), and $\frac{\gamma}{2\pi} = 28$ GHz/T is the electron spin gyromagnetic ratio. To a good approximation, the drive field B_{AC} generated by the stripline is normal to the sample plane at the NV site. Therefore, the total field amplitude at the NV site B_{AC} can be related to the Rabi frequency using

$$B_{\text{AC}} = \frac{B_{\text{AC}\perp}}{\sin\theta} = \frac{2\pi\sqrt{2} f_{\text{R}}}{\gamma \sin\theta} \quad \text{(S1)}$$

where θ is the angle of the NV axis relative to the sample normal. By tuning the ESR frequency using a DC magnetic field and measuring the Rabi frequency at each field value,

we can probe the setup transmission over the entire frequency range of interest (Fig. S3B). We use this calibration curve to adjust the output power of the MW source for each desired frequency and achieve a constant (i.e., frequency-independent) magnetic-field amplitude on the chip.

Section S2. Measuring the NV spin relaxation rates

Measuring the NV spin relaxation rates plays a central role in this work, allowing us to probe the spectral density of magnons at the NV ESR frequencies (as described by Eq. 1 in the main text). To measure the NV relaxation rates, we use the pulse sequence depicted in Fig. 2A of the main text: we initialize the NV spin in the $m_s = 0$ state, and let the system relax for a time t. At the end of this time, we measure the spin-dependent photoluminescence either directly ($m_s = 0$ readout), or after applying a pi pulse on the $m_s = 0 \leftrightarrow -1$ transition ($m_s = -1$ readout), or after applying a pi pulse on the $m_s = 0 \leftrightarrow +1$ transition ($m_s = +1$ readout). An illustrative measurement is shown in Fig. S4A.

To extract the relaxation rates from these measurements, we fit the data using the following rate equations, which are based on the three level model depicted in Fig. S4B (*24*):

$$\frac{d}{dt}\begin{pmatrix} P_0(t) \\ P_+(t) \\ P_-(t) \end{pmatrix} = \begin{pmatrix} -(\Gamma_+ + \Gamma_-) & \Gamma_+ & \Gamma_- \\ \Gamma_+ & -\Gamma_+ & 0 \\ \Gamma_- & 0 & -\Gamma_- \end{pmatrix}\begin{pmatrix} P_0(t) \\ P_+(t) \\ P_-(t) \end{pmatrix} \quad \text{(S2)}$$

Here, P_0, P_+, and P_- are the probabilities of the NV spin to be in the $m_s = 0$, $m_s = +1$, and $m_s = -1$ states respectively, and Γ_+ and Γ_- are the spin relaxation rates of the $m_s = 0 \leftrightarrow +1$ and $m_s = 0 \leftrightarrow -1$ transitions respectively. Note that we set the rate between the $m_s = +1$ and $m_s = -1$ states to zero, which is justified as this rate is unaffected by magnetic noise (to first order) and is much smaller than Γ_+ and Γ_- for all measurements presented in this work (on the order of 1/ms (see supplement of (*36*)).

Section S3. Relating the NV spin relaxation rates to the magnetic-field noise generated by magnons in the YIG film

The magnetic fields generated by magnons at the NV ESR frequencies induce NV spin relaxation as described by Eq. 1 in the main text. In this section we describe the full version of this equation, which was used to fit the measurement of the NV spin relaxation rates presented in Fig. 2A of the main text and in Figs. S4C-D.

The equation for the NV relaxation rates that forms the starting point for deriving Eq. 1 is given by

$$\Gamma_\pm(\mu) = \iint n(\omega,\mu) D(\omega,\mathbf{k}) f(\mathbf{k},d) \mathrm{g}(\omega-\omega_\pm) \mathrm{d}\mathbf{k}\, \mathrm{d}\omega + \Gamma_\pm^0,$$

where $n(\omega,\mu) = \frac{k_B T}{\hbar\omega - \mu}$ is the Rayleigh-Jeans distribution, and the function $\mathrm{g}(\omega-\omega_\pm)$ is the 'energy filter function' of the NV center, which reflects that the NV relaxation rates $\Gamma_\pm$ are only sensitive to magnetic noise at the NV ESR frequencies $\omega_\pm$. Because the NV ESR linewidths are much narrower than any features of the rest of the integrand (which is described in more detail below), we can model $g(\omega-\omega_\pm)$ as a delta function centered at

the NV ESR frequency. This allows us to perform the integral over frequency, resulting in Eq. 1:

$$\Gamma_{\pm}(\mu) = n(\omega_{\pm}, \mu) \int D(\omega_{\pm}, \mathbf{k}) f(\mathbf{k}, d) \mathrm{d}\mathbf{k} + \Gamma_{\pm}^{0} \quad \text{(S3)}$$

We model the magnon spectral density $D(\omega_{\pm}, \mathbf{k}) = \frac{1}{\pi} \frac{W}{W^2 + [\omega(k,\phi_k) - \omega_{\pm}]^2}$ as a Lorentzian function centered at the magnon dispersion $\omega(k, \phi_k)$ (see Section S4), where k and ϕ_k are polar coordinates describing the magnon wavevector **k,** with ϕ_k the azimuthal angle relative to the y axis (Fig. S5A). We take W equal to the measured width of the ferromagnetic resonance (see inset of Fig. 2C of the main text). The transfer function $f(\mathbf{k}, d)$ describes the magnon-generated fields at the NV site causing NV spin relaxation, with d the distance of the NV to the top surface of the YIG film (*24*):

$$f(\mathbf{k}, d) = C\, k e^{-2dk} \left(1 - e^{-2t_{\mathrm{YIG}}k}\right) \left[\sin^4\left(\phi_k\right) + \cos^2(\theta) \frac{\sin^2\left(2\phi_k\right)}{4} + \sin^2(\theta) \sin^2\left(\phi_k\right)\right] \quad \text{(S4)}$$

where C is a constant, θ is the angle of the NV axis with respect to the normal of the sample surface, and t_{YIG} is the thickness of the YIG film. The term $k e^{-2dk}\left(1 - e^{-2t_{\mathrm{YIG}}k}\right)$ is a 'filter function' (*24*), describing the range of magnons that generate a field outside the YIG film (note that the uniform mode with $k = 0$ does not generate a magnetic field, and modes with $k \gg d$ are exponentially suppressed). The term between square brackets in Eq. S4 calculates the field components perpendicular to the NV axis, which are the ones causing spin relaxation (*24*). We note that this model assumes in-plane magnetization fluctuations to be dominant because out-of-plane fluctuations are suppressed by the demagnetizing field, particularly for low magnon wavenumbers for which the precessional motion is known to be highly elliptic (*37*). Analyzing the wavenumber-dependency of the ellipticity may provide a route for improving this model. Summarizing, the full expression for $\Gamma_{\pm}(\mu)$ is given by

$$\Gamma_{\pm}(\mu) = C \frac{k_B T}{\hbar\omega_{\pm} - \mu} \int \left(\sin^4\left(\phi_k\right) + \cos^2(\theta) \frac{\sin^2\left(2\phi_k\right)}{4} + \sin^2(\theta) \sin^2\left(\phi_k\right)\right) \frac{W k e^{-2dk}\left(1 - e^{-2t_{\mathrm{YIG}}k}\right)}{\pi\left\{W^2 + [\omega(k,\phi_k) - \omega_{\pm}]^2\right\}} k \mathrm{d}k \mathrm{d}\phi_k + \Gamma_{\pm}^{0} \quad \text{(S5)}$$

We use this equation to fit the measurements presented in Fig. 2A of the main text and in Fig. S4C. The dependence on the external magnetic field B_{ext} enters through the NV ESR frequencies $\omega_{\pm} = D \pm \gamma B_{\mathrm{ext}}$, where $\frac{D}{2\pi} = 2.87$ GHz is the NV zero-field splitting, and through the field-dependent magnon dispersion (see Section S4). This model agrees well with the measured field dependence for both NV_1 and NV_2. We note that the only fitting parameters are the global amplitude C and the NV distance above the film d.

Section S4. Magnon dispersion of the 20 nm YIG film

In this section we describe the magnon dispersion $\omega(k, \phi_k)$ of the 20 nm YIG film used for the experiments described in this work. We follow the formalism presented in the classic work by Kalinikos and Slavin (*38*).

In all experiments presented in this work, we apply B_{ext} along the axis of the NV center under the study, i.e., at an angle θ with respect to the YIG film normal. We define a coordinate system such that B_{ext} lies in the yz plane (Fig. S5A). The first task in calculating the magnon dispersion is to calculate the magnetic field inside the YIG film (the 'internal field'). The angle $\theta_{\mathrm{n_0}}$ and magnitude $B_{\mathrm{n_0}}$ of the internal field differ from the angle and

magnitude of the external field because of the demagnetizing field that is generated by an out-of-plane component of the magnetization, which opposes the component of B_{ext} perpendicular to the film. The internal field $B_{\mathrm{n_0}}$ can be found (*38*) by solving

$$B_{\mathrm{n_0}}\cos\left(\theta_{\mathrm{n_0}}\right) = B_{\mathrm{ext}}\cos(\theta) - \mu_0 M_{\mathrm{s}}\cos\left(\theta_{\mathrm{n_0}}\right) \quad \text{(S6)}$$

$$B_{\mathrm{n_0}}\sin\left(\theta_{\mathrm{n_0}}\right) = B_{\mathrm{ext}}\sin(\theta) \quad \text{(S7)}$$

where $\mu_0 = 4\pi \cdot 10^{-7}$, and M_{s} is the saturation magnetization of the YIG film (we use SI units). Note that the angle $\theta_{\mathrm{n_0}}$ is equal to the angle of the static magnetization.

Figure S5B shows the angle $\theta_{\mathrm{n_0}}$ for a 20 nm YIG film as a function of B_{ext} at $\theta = 65°$ (corresponding to the angle of the axis of NV_1 and NV_2). We use this to calculate $\cos(\theta_{\mathrm{n_0}})^2$ which is presented in Fig. S5C. In the Section S5, this term is used to calculate chemical potential induced by FMR driving. Following ref. (*38*), the internal field can subsequently be used to calculate the magnon dispersion

$$\omega(k,\phi_k) = \sqrt{\left(\gamma B_{\mathrm{n_0}} + \frac{D_{\mathrm{s}}}{\hbar}k^2\right)\left(\gamma B_{\mathrm{n_0}} + \frac{D_{\mathrm{s}}}{\hbar}k^2 + \gamma\mu_0 M_{\mathrm{s}} F(k,\phi_k)\right)} \quad \text{(S8)}$$

where $D_{\mathrm{s}} = 1.00 \cdot 10^{-39}\,\mathrm{J}\cdot\mathrm{m}^2$ (*38*) is the YIG spin stiffness, and

$$F(k,\phi_k) = P(k) + \sin^2\left(\theta_{\mathrm{n_0}}\right)\left(1 - P(k)(1+\cos^2\phi_k) + \gamma\mu_0 M_{\mathrm{s}}\frac{P(k)(1-P(k))\sin^2\phi_k}{\gamma B_{\mathrm{n_0}} + \frac{D_{\mathrm{s}}}{\hbar}k^2}\right) \quad \text{(S9)}$$

where $P(k) = 1 - \frac{\left(1-e^{-kt_{\mathrm{YIG}}}\right)}{kt_{\mathrm{YIG}}}$.

To fit the data in Fig. 2A of the main text, we substitute the magnon dispersion given by Eq. S8 into Eq. S5. We note that the sketches of the magnon dispersion shown in Figs. 1B-C in the main text were also calculated using these equations. As an example, Fig. S5D shows the magnon dispersion of our 20 nm YIG film at B_{ext} = 15 mT. The blue (red) curve represents the dispersion of magnons that travel perpendicularly (parallelly) to the in-plane projection of the magnetization (i.e., magnons with $\phi_k = 90°$ ($\phi_k = 0°$)). The grey curve is the 'filter function' $ke^{-2dk}(1 - e^{-2t_{\mathrm{YIG}}k})$ (see Eq. S4), illustrating the range of magnons that produce magnetic fields outside the YIG film and can thus be detected by the NV center. Finally, we note that the minimum frequency of the magnon band of our 20 nm YIG film is essentially the same as the FMR frequency over the field range probed in our experiments (Fig. S5E), in contrast with micrometer-thick films (*38*).

For calculating the k = 0 ferromagnetic resonance frequency ω_{FMR}, Eqs. S8-S9 reduce to a simple form:

$$\omega_{\mathrm{FMR}} = \gamma\sqrt{B_{\mathrm{n_0}}\left(B_{\mathrm{n_0}} + \mu_0 M_{\mathrm{s}}\sin^2\left(\theta_{\mathrm{n_0}}\right)\right)} \quad \text{(S10)}$$

We use this equation to fit the field dependence of the FMR extracted from the measurement presented in Fig. 2C of the main text, using the saturation magnetization of the YIG film M_{s} as the only free parameter. We find $M_{\mathrm{s}} = 1.24 \cdot 10^5$ A/m.

Section S5. Generation of incoherent magnon gas under ferromagnetic resonance excitation

In this section we give a derivation of Eqs. 3 and 4 in the main text. We begin by formulating a set of phenomenological equations describing the coupled dynamics of the incoherent magnon gas and the coherent spin order parameter. Let us specifically consider a thin film of a magnetic insulator at a finite temperature (Fig. S5A). The hydrodynamic variables that describe this system are the three-component coherent spin density $s\mathbf{n} \equiv s(n_x, n_y, n_z)$ and the density of an incoherent gas of magnons $\tilde{n}$ (in units of one per unit volume). Here, s is the magnitude of the coherent spin density (in units of angular momentum per unit volume) and $\mathbf{n}$ is a unit vector (Fig. S5A). Microscopically, the coherent part represents the expectation value of the total spin density operator $\hat{\mathbf{s}}$, i.e. $s\hat{\mathbf{n}} \equiv \langle\hat{\mathbf{s}}\rangle$, while the incoherent magnons describe the fluctuations $\delta s = s - \langle\hat{\mathbf{s}}\rangle$.

The free energy density describing our system can be written in terms of these hydrodynamic variables as: $F(\mathbf{n}, \tilde{n}) \equiv F_{\mathbf{n}} + F_{\tilde{n}}$. Here, the effective magnetic field, $\mathrm{H} \equiv \delta_{\boldsymbol{n}} F_n$, and the chemical potential, $\mu \equiv \delta_{\tilde{n}} F_{\tilde{n}}$, are the thermodynamic forces conjugate to $\mathbf{n}$ and $\tilde{n}$, respectively. The incoherent magnon gas is described by a well-defined chemical potential and temperature under the assumption that the interactions within the incoherent magnon gas are strong enough to quasi-equilibrate them to a Bose-Einstein profile. Within linear response, the coupled dynamics are then described by:

$$\begin{pmatrix} \dot{\mathbf{n}} \\ \dot{\tilde{n}} \end{pmatrix} = \begin{pmatrix} \mathbf{L^{nn}} & \mathbf{L^{n\tilde{n}}} \\ \mathbf{L^{\tilde{n}n}} & L^{\tilde{n}\tilde{n}} \end{pmatrix} \begin{pmatrix} \mathbf{H} \\ \mu \end{pmatrix} \tag{S11}$$

The kinetic coefficients $\mathbf{L^{nn}}$ and $L^{\tilde{n}\tilde{n}}$ describe respectively the decoupled dynamics of the coherent sector and the incoherent magnon gas. Here, we are specifically interested in the coupling between the coherent and the incoherent sectors, as encoded in $\mathbf{L^{n\tilde{n}}}$, describing the local thermomagnonic torque on the coherent magnetization dynamics, and $\mathbf{L^{\tilde{n}n}}$, describing the pumping of incoherent magnon gas due to coherent magnetization dynamics.

S5.1 Decoupled dynamics

Before we derive the local thermomagnonic torque and magnon pumping, we write the decoupled equation of motion. For the coherent part, $\mathbf{L^{nn}}$ is given by the Landau-Lifshitz-Gilbert equation:

$$\mathrm{s}(1 + \alpha\mathbf{n}\times)\dot{\mathbf{n}} = \mathbf{H} \times \mathbf{n} \tag{S12}$$

Here, α is the Gilbert damping coefficient associated with the transfer of angular momentum to the atomic lattice. The kinetic coefficient for the incoherent magnon gas can be obtained from the continuity equation for magnon transport (*9*):

$$\dot{\tilde{n}} = -\boldsymbol{\nabla}\cdot\mathbf{j} - \frac{\tilde{\alpha}\mathrm{s}\mu}{\hbar^2} \tag{S13}$$

Here, $\mathbf{j} \equiv -\sigma\boldsymbol{\nabla}\mu$ is the magnon current density with σ the magnon conductivity. The first term on the right-hand side represents the drift of magnons in response to a gradient of the chemical potential, while the second term describes the decay of magnons to the atomic lattice. The second term can be derived using the Boltzmann equation in the relaxation time approximation (*39*). For small deviations of the magnon distribution function f from its equilibrium state f_0 we have

$$\dot{f} = \frac{f - f_0}{\tau} = \frac{\mu}{\tau}\left[\frac{\partial f_0}{\partial \mu}\right]_{\mu=0} \tag{S14}$$

with $f_0 = \frac{1}{e^{\frac{(E-\mu)}{k_B T}} - 1}$ the Bose-Einstein distribution function, and $\tau = \frac{\hbar}{2\alpha E}$ the magnon-lattice relaxation time associated with the Gilbert damping parameter α. The time evolution of the incoherent magnon density is given by

$$\dot{\tilde{n}} = \int_0^\infty \dot{f} g(E) dE \tag{S15}$$

with $g(E)$ the density of states. Assuming a parabolic magnon dispersion with $E(k) = D_s k^2$, the density of states is $g(E) = \frac{1}{2\pi^2}\left(\frac{2m}{\hbar^2}\right)^{\frac{3}{2}} E^{\frac{1}{2}}$ with $m = \frac{\hbar^2}{2D_s}$ the effective magnon mass. Substituting Eq. S14 into Eq. S15, we get

$$\dot{\tilde{n}} = \frac{\alpha I s \mu}{\hbar^2}\left(\frac{T}{T_c}\right)^{\frac{3}{2}} = \frac{\tilde{\alpha} s \mu}{\hbar^2} \tag{S16}$$

where we define $\tilde{\alpha} = \alpha I \left(\frac{T}{T_c}\right)^{\frac{3}{2}}$, $I = \frac{1}{\pi^2}\int_0^\infty dx \frac{x^{3/2} e^x}{(e^x - 1)^2}$, and $T_c = \frac{D_s}{k_B}\left(\frac{s}{\hbar}\right)^{\frac{2}{3}}$. Further background on this procedure can be found in (*9*) and its supplemental material.

S5.2 Coupled dynamics

We next write down the form of $\mathbf{L}^{\mathbf{n}\tilde{n}}$ and $\mathbf{L}^{\tilde{n}\mathbf{n}}$, which can in general depend on the orientation **n,** as dictated by the symmetries of the system. Firstly, Onsager reciprocity demands that the local thermomagonic torque and the pumping of incoherent magnons are reciprocal to each other, i.e. (*40*):

$$\mathbf{L}^{\mathbf{n}\tilde{n}}(\mathbf{n}) = -\mathbf{L}^{\tilde{n}\mathbf{n}}(-\mathbf{n}) \tag{S17}$$

Thus, once $\mathbf{L}^{\mathbf{n}\tilde{n}}$ is known we can immediately obtain $\mathbf{L}^{\tilde{n}\mathbf{n}}$ from the above condition. To obtain $\mathbf{L}^{\mathbf{n}\tilde{n}}$, we note that since the magnitude of **n** is not a dynamic degree of freedom, the equation of motion for **n** due to local thermomagnonic torque, takes the form:

$$\hbar \dot{\mathbf{n}} = \mathbf{n} \times \mathbf{h}_*(\mu, \mathbf{n}) \tag{S18}$$

where $\mathbf{h}_*(\mu, \mathbf{n})$ depends on the orientation **n** and the nonequilibrium variable μ. In general, $\mathbf{h}_*$ may also depend on $\dot{\mathbf{n}}$, describing damping of the coherent spin density due to the coupling to incoherent magnons (*29*). Motivated by constructing a minimal model for explaining the buildup of the chemical potential for the present experimental setup, we neglect such damping terms here. We next use the fact that Eq. S18 should remain invariant under the structural symmetries. For the thin YIG films under consideration, these symmetry transformations are arbitrary rotations about the *z* axis and reflection through any mirror plane perpendicular to the *xy*, *yz* and *xz*-planes. Imposing this invariance condition and noting that **n** transforms as a pseudovector, we can, expand $\mathbf{h}_*(\mu, \mathbf{n})$ within linear response up to linear order in μ to get:

$$\hbar \dot{\mathbf{n}} = \mu \eta_n(\theta_n) \mathbf{n} \times (\mathbf{n} \times \mathbf{z}) \tag{S19}$$

with $\eta_n(\theta_n) = -\eta_n(\pi - \theta_n)$, and θ_n the instantaneous angle between the *z* axis and **n**, and **z** is a unit vector along the normal of the film plane (Fig. S5A).

The appearance of **z** in Eq. S19 originates from the rotational symmetry about the *z* axis, while the condition of η_n being odd about $\theta_n = \pi/2$ can be obtained by invoking the mirror symmetry about the *yz* plane. In addition, a term of the form $\dot{\mathbf{n}} \sim \mathbf{n} \times \mathbf{z}$ is also allowed, which is a field-like torque whose Onsager reciprocal will however not pump any magnons (*29*). We thus neglect it here. Combined with Eq. S11, it follows from Eq. S19 that $\mathbf{L}^{\mathbf{n}\tilde{n}} = (\eta_n/\hbar)\ \mathbf{n} \times (\mathbf{n} \times \mathbf{z})$. In analogy to spin current-induced torques (*31*), this term is interpreted as the anti-damping-like local thermomagnonic torque, whose strength is

parameterized by η_n (referred to here as the coupling between the coherent spin density and the magnons). Such form of anti-damping torque has been derived microscopically for the special case of $\theta_n = 0$ and has been attributed to arise from the breaking of SU(2) symmetry by a non-zero anisotropy of the form $K\hat{s}_z^2$ (*27*). Equation S19 generalizes the anti-damping local thermomagnonic torque for arbitrary θ_n. In particular, the coupling between the coherent spin density and the incoherent magnons goes to zero for an in-plane orientation of the coherent spin density, i.e., for $\theta_n = \pi/2$. Microscopically, the SU(2) symmetry-breaking term $K\hat{s}_z^2$ can only couple the coherent spin density to magnons carrying angular momentum along the z axis. For the in-plane orientation, the magnons have no net angular momentum along the z axis and become decoupled from the coherent order parameter.

Next, applying the Onsager reciprocal relation, Eq. S17, to Eq. S11 we immediately get the pumping of incoherent magnons by the coherent dynamics of the spin order parameter:

$$\dot{\tilde{n}} = \eta_n(\theta_n)\frac{s}{\hbar}\mathbf{z}\cdot(\dot{\mathbf{n}}\times\mathbf{n}) \tag{S20}$$

where we have used $\mathbf{H} = s\mathbf{n}\times\dot{\mathbf{n}}$ by inverting Eq. S12 within linear response.

We now specialize to the experimentally relevant case of $\theta_n \approx \pi/2$ and write $\eta_n(\theta_n) = \eta\cos\theta_n$ in the following. Combining the decoupled (Eq. S13) and the coupled dynamics (Eq. S20), and assuming $\boldsymbol{\nabla}\mu = 0$, we obtain the following hydrodynamic equation for the incoherent magnon density:

$$\dot{\tilde{n}} = -\frac{\tilde{\alpha}s\mu}{\hbar^2} + \eta\cos\theta_n\frac{s}{\hbar}\mathbf{z}\cdot(\dot{\mathbf{n}}\times\mathbf{n}) \tag{S21}$$

which is the same as Eq. 3 of the main text.

The steady-state chemical potential for the FMR-induced precession of $\mathbf{n}$ near the in-plane equilibrium orientation can be obtained by balancing the loss of magnons to the lattice and the generation of magnons by pumping (i.e., we set $\dot{\tilde{n}} = 0$), and averaging Eq. S21 over the precession cycle. To perform the average, we express $\mathbf{n}$ in a rotated coordinate system (indicated by primed variables), with z' aligned with the equilibrium orientation of the magnetization (Fig. S5A):

$$\mathbf{n}\approx(n_x', n_y', 1-\tfrac{(n_x')^2+(n_y')^2}{2}) \tag{S22}$$

Here $n_x' = \delta n_1\sin(\omega_{FMR}t)$, $n_y' = \delta n_2\cos(\omega_{FMR}t)$, with ω_{FMR} the precession frequency, and δn_1 and δn_2 are the (small) transverse amplitudes of the elliptical precession of the coherent spin density induced by the resonant FMR field. Furthermore, we have used $\sqrt{1-(n_x')^2-(n_y')^2} \approx 1-\frac{(n_x')^2+(n_y')^2}{2}$. Transforming the other parameters in Eq. S21 to the rotated coordinate system, we get (up to leading order in small amplitudes):

$$\dot{\mathbf{n}} \approx (\dot{n}_x', \dot{n}_y', -n_x'\dot{n}_x' - n_y'\dot{n}_y') \tag{S23}$$

$$\mathbf{z} = (0, -\sin\theta_{n_0}, \cos\theta_{n_0}) \tag{S24}$$

$$\cos\theta_n = \mathbf{n}\cdot\mathbf{z} = -n_y'\sin\theta_{n_0} + \cos\theta_{n_0} \tag{S25}$$

$$\dot{\mathbf{n}}\times\mathbf{n} \approx (\dot{n}_y', -\dot{n}_x', n_y'\dot{n}_x' - n_x'\dot{n}_y') \tag{S26}$$

Using these relations, we can average the dynamics over a full precession cycle. There are two extreme regimes for performing such averaging: (a) the non- adiabatic regime and (b) the adiabatic regime. The non-adiabatic regime holds when the precession frequency of $\mathbf{n}$ is much faster than the pumping-induced change in magnon population. When averaging over the precession cycle, the coupling η is assumed to take on its average value, i.e.

$\langle \eta_n(\theta_n) \rangle = \eta_n(\theta_{n_0})$. Combined with Eqs. S21-S26, the resulting chemical potential in the non-adiabatic regime is given by

$$\mu = \langle \mu \rangle = \frac{\hbar \langle \eta \cos\theta_n \rangle \langle \mathbf{z} \cdot (\dot{\mathbf{n}} \times \mathbf{n}) \rangle}{\tilde{\alpha}} = \frac{\hbar \omega_{FMR} \eta \, \delta n_1 \delta n_2 \cos^2 \theta_{n_0}}{\tilde{\alpha}} \quad \text{(S27)}$$

Equation S27 with its $\mu \sim \cos^2 \theta_{n_0}$ dependence, describes the experimental observations presented in Fig. 4E of the main text very well (See Fig. S5C for the calculated value of $\cos^2 \theta_{n_0}$). Substituting $\delta n_1 = \gamma B_{AC} \sin\theta_{n_0}/(2\alpha\omega_1)$ and $\delta n_2 = \gamma B_{AC} \omega_H \sin\theta_{n_0}/(2\alpha\omega_{FMR}\omega_1)$, with $\omega_H = \gamma[B_{ext} \cos(\theta_{n_0} - \theta) - \mu_0 M_s \cos^2 \theta_{n_0}]$ and $\omega_1 = \omega_H + \frac{\mu_0 \gamma M_s}{2} \sin^2 \theta_{n_0}$ (*37*), we obtain the central result of this section:

$$\mu = \frac{\eta \hbar \omega_H \gamma^2 \sin^2 \theta_{n_0}}{4\tilde{\alpha}\alpha^2 \omega_1^2} B_{AC}^2 \cos^2 \theta_{n_0} \quad \text{(S28)}$$

Defining $\kappa = \frac{\hbar \omega_H \gamma^2 \sin^2 \theta_{n_0}}{4\alpha^2 \omega_1^2}$, Eq. S28 reduces to $\mu = \kappa \frac{\eta}{\tilde{\alpha}} B_{AC}^2 \cos^2 \theta_{n_0}$, which is the same as Eq. 4 in the main text. Fitting the dependence of the drive efficiency $d\mu/dB_{AC}^2$ on B_{ext} in the low-power regime (Fig. 3E) to Eq. S28, we obtain the value of η. Finally, we note that future studies that more fully include the complex YIG band structure, as well as a possible energy dependence of damping, may improve the determination of η.

For the opposite adiabatic regime, the chemical potential is given by $\langle \mu \rangle = \hbar\eta \langle \cos\theta_n \mathbf{z} \cdot (\dot{\mathbf{n}} \times \mathbf{n}) \rangle / \tilde{\alpha} = \hbar\eta(\cos^2 \theta_{n_0} \omega_{FMR} \delta n_1 \delta n_2 - \sin^2 \theta_{n_0} \omega_{FMR} \delta n_1 \delta n_2/2)/\tilde{\alpha}$. In the near in-plane orientation we are probing, the $\sin^2 \theta_{n_0}$ term dominates, which is however inconsistent with our observations.

Section S6. Effect of temperature under ferromagnetic resonance excitation

We attribute the increase in relaxation rate observed in Fig. 3A in the main text to a change in chemical potential (Fig. 3B in the main text). Importantly, we rule out that this increase results from a change in magnon temperature induced by the FMR drive field, as we will describe in this section. We will analyze both the change in magnon temperature and the change in phonon temperature under FMR drive, in Sections S6.1 and S6.2 respectively.

S6.1 Magnon temperature

In this section we present measurements that provide an upper bound on the increase in magnon temperature under FMR drive. In summary, we measure this increase to be ≤ 5 K at the highest drive power used in Fig. 3 of the main text, from which we can safely conclude that an increase in magnon temperature does not play a significant role in the Fig. 3 measurements. Nevertheless, we recalculate the chemical potential taking this upper-bound estimate of the increase in magnon temperature into account to clearly demonstrate that the effect is negligible.

A key point of our argument is that an increase in magnon temperature would reduce the YIG saturation magnetization M_S. We can thus assess the change in magnon temperature under FMR drive by monitoring the shift in M_S. Figure S6A shows a measurement of the shift of ω_{FMR} as a function of the FMR drive power B_{AC}^2. Using Eq. S10, we convert this shift to a change in M_S (Fig. S6B). We observe that M_S is slightly

reduced by 1.5% at the highest drive power. Then, assuming that this reduction results entirely from a change in magnon temperature, we invert Bloch's 3/2 law

$$M_s(T) = M_0\left[1 - (T/T_c)^{3/2}\right] \tag{S29}$$

where M_0 is the saturation magnetization at T = 0 K, T_c = 550 K is the YIG Curie temperature, and where we calculate M_0 from the measured $M_s = 1.24 \cdot 10^5$ A/m at room temperature, to obtain an upper-bound estimate of the increase in magnon temperature (Fig. S6C). We thus estimate that at the highest drive power used in the measurements of Fig. 3 of the main text, the magnon temperature increases by less than $\Delta T_{\max} = 5$ K.

To independently confirm the validity of this estimate, we perform additional measurements in which we use our on-chip platinum wire as a resistive heater. Using our NV sensor, we measure both the change in ω_{FMR} and the local YIG temperature as a function of the DC current density J_c in the wire (Fig. S6D-E). For both measurements we observe a quadratic dependence on J_c as expected for resistive heating. Combining Figs. S6D-E, we obtain a calibration curve relating the change in ω_{FMR} to a change in temperature (Fig. S6F). We find that ω_{FMR} shifts at a rate of ~-2 MHz/K. We then use this rate to convert the measured FMR-drive-induced change of ω_{FMR} (Fig. S6A) to a temperature change (Fig. S6C). We find a good agreement with the temperature change determined using the Bloch 3/2 law (Fig. S6C).

Next, we assume that the magnon temperature under FMR drive increases in accordance with our upper-bound estimate and analyze if such an increase could play a significant role in the measurements of the NV relaxation rates and extracted chemical potentials presented in Fig. 3 of the main text. To start, we note that a temperature change affects the NV relaxation rates (described by Eq. 1 of the main text) in two ways: 1) through the Rayleigh-Jeans factor and 2) through the spectral density D, which depends on the magnetization, which in turn depends on temperature (as described in Sections S3 and S4). Intuitively, we may already anticipate that the change in magnon temperature does not significantly affect the measured NV relaxation rates, because both the magnon temperature itself and the associated magnetization change by less than 2% even at the highest drive power (Figs. S6B-C), while the observed changes in relaxation rate are ≥ 200% (Fig. 3A of the main text). To be more quantitative, we reformulate Eq. 1 of the main text as

$$\Gamma_{\pm}(\mu, \Delta T) = \Gamma_{\pm}(0,0)\frac{(1+b\Delta T)}{1-\frac{\mu}{\hbar\omega_{\pm}}} \tag{S30}$$

where we have linearized the temperature dependence using the constant b and we neglected $\Gamma_{\pm}^0$. This linearization is justified over the range $0 < \Delta T < \Delta T_{\max}$, as we conclude from both a numerical analysis of Eq.1 and a consistent, independently measured change in relaxation rate as a function of the sample temperature controlled by the Pt wire (Fig. S7A). In Fig. S7A, we observe that the increase in temperature only reduces the rate by a small amount. For example, for our upper-bound estimate of the maximum change in magnon temperature under FMR drive ($\Delta T_{\max} = 5$ K), we see that $b\Delta T_{\max} = -3\%$.

Solving Eq. S30 for the chemical potential, we obtain the temperature-adjusted version of Eq. 2 of the main text,

$$\mu = \omega_{\pm}\hbar \left[1 - (1 + b\Delta T)\frac{\Gamma_{\pm}(0,0)}{\Gamma_{\pm}(\mu,\Delta T)}\right] \quad \text{(S31)}$$

which we can use to calculate the chemical potential taking into account a FMR-drive-induced temperature change. Figure S7B shows a comparison of the original values of chemical potential (solid markers, calculated with Eq. 2 of the main text) and the corrected chemical potential values that include our upper-bound estimate for the drive-induced magnon-temperature change (empty markers outlined in black, calculated with Eq. S31), at three different fields. We don't observe a significant difference. We conclude that we can safely neglect the effect of a potential FMR-drive-induced change in magnon temperature on our measurements.

S6.2 Temperature at the NV site

In this section we show that the phonon temperature at the NV site does not change significantly under the application of an FMR drive field. We quantify the temperature by measuring the NV zero-field splitting D as a function of driving power B_{AC}^2 (Fig. S8A). From previous work (*41*), we know that D changes with temperature at a rate of -78.6 KHz/K, allowing us to convert the change in D to a change in temperature T (Fig. S8B). We assume this temperature to be equal to the local YIG phonon temperature because of the high thermal conductivity of diamond and the relatively insulating properties of air. Figure S6B shows that, within a ~1 K uncertainty, there is no significant change of temperature over the entire range of drive powers used in Fig. 3A-B in the main text. Moreover, the control measurement in Figs. S8A-B is performed under continuous FMR driving and therefore overestimates the temperature change that may occur during the measurements in Fig. 3A-B in the main text, which are performed with a finite duty cycle with on average ~50% power-off time. Therefore, we conclude that even at the highest FMR drive power, the phonon temperature increase in our system is less than ~ 1 K.

Section S7. Analysis of the effect of thermal heating on the NV relaxation rate in the spin-Hall measurements.

In the spin-Hall effect measurements, we attribute the quadratic part of the change in relaxation rate (red curve in Fig. 4B of the main text) to heating by Ohmic dissipation in the Pt wire. To calculate the effect of heating on the NV relaxation rate, we first quantify the current-induced temperature change by measuring the variation of the NV zero-field splitting D (Fig. S9A). Figure S9B shows the corresponding change in temperature (T) by converting D to T (*41*). The temperature change is proportional to J_c^2 as expected for Ohmic dissipation. The measured temperature change at the maximum current density J_c $=1.2\times10^{11}$A/m^2 is about 40 K.

The increase in temperature reduces the YIG saturation magnetization M_S. as described by Bloch's Law (Eq. S29), shown in Fig. S9C. Knowing the change in M_s, we can calculate the change in NV relaxation rate Γ_- using Eq. S5 (Fig. S9D), where we use the values of C and d determined from the fit to the data in Fig. 2B in the main text. We observe that the relaxation rate decreases with decreasing M_s. This can be explained by noting that the reduction in M_s shifts the entire magnon band down in frequency. As a result, the NV ESR frequency becomes resonant with magnons having a larger wavenumber which, in the field region we are probing, generate less magnetic noise at the

NV-site as described by the 'filter function' shown in Fig. S5D. Combining the results from Figs. S9C-D, we obtain the calculated temperature and current-density dependence of Γ_- (Figs. S9E-F). A comparison to the measured data shows an excellent agreement (Fig. S9F), illustrating the powerful potential of using NV spins to study temperature-related magnon phenomena such as the spin Seebeck effect (*11*).

Section S8. Analysis of the effect of the DC magnetic field generated by the current in the Pt stripline on the NV relaxation rate

As described in the main text, we attribute the linear component of the change in relaxation rate observed in Fig. 4C of the main text to the spin-Hall effect (SHE). We rule out a possible contribution of the DC field B_{Pt} generated by the current in the Pt stripline using two control measurements, which we describe in this section.

As the NV ESR frequencies are sensitive to magnetic fields along the NV axis, our NV sensor allows a straightforward, in-situ measurement of the component $B_{\mathrm{Pt}//} = B_{\mathrm{Pt}}\cos(\theta)$ (Fig. S10A) by measuring the NV ESR frequencies and using the relation $B_{\mathrm{Pt}}\cos(\theta) = \frac{\omega_+ - \omega_-}{2\gamma} - B_{\mathrm{ext}}$. We see that this current generates a small field of about 0.1 mT (Fig. S10B). To rule out that this field induces the linear change in the relaxation rate observed in Fig. 4C of the main text, we perform a control experiment at zero current through the Pt. In this experiment, we move our external magnet along a calculated trajectory, such that we precisely replicate the change in field created by the current in the Pt in both direction and magnitude (i.e., $\Delta\mathbf{B}_{\mathbf{ext}} = \mathbf{B}_{\mathbf{Pt}}$). While doing so we do not discern a significant change of Γ_- (Fig. S10C) over the relevant field range. At the maximum current density ($J_c = 1.2 \times 10^{11}\ \mathrm{A/m^2}$), the change of rate due to B_{Pt} is estimated to be $(2\pm4) \times 10^{-4}\ \mu\mathrm{s}^{-1}$, which is not significantly different from zero and over an order of magnitude smaller than the measured linear part of the rate change shown in Fig. 4C of the main text, which is $(5.5\pm1.1) \times 10^{-3}\ \mu\mathrm{s}^{-1}$ (see also Fig. S10C). We conclude that the current-induced change in relaxation rate is not caused by B_{Pt}.

To further validate this conclusion, we also measure the NV relaxation rate as a function of current through the Pt stripline at a much higher external field of $B_{\mathrm{ext}} = 65$ mT (Fig. S10D). As in Fig. 4C of the main text, we observe that the linear component increases in the positive current direction. Since we know that a positive current increases the total field (as reflected by the sign of $B_{\mathrm{Pt}//}$ in Fig. S10B) and that the NV relaxation rate actually decreases for increasing B_{ext} in this field range (Fig. S10E), we conclude that the observed increase in NV relaxation rate cannot result from B_{Pt}.

Section S9. Analyzing the chemical potential under spin-Hall injection

S9.1 Extracting the chemical potential from the measured NV relaxation rates

In Fig. 4C of the main text, we extract the chemical potential induced by the spin Hall effect (SHE) from the linear component of the change in relaxation rate. In this section, we describe this procedure in detail.

Equation 1 of the main text can be written as

$$\Gamma_- = \frac{G(T)}{\hbar\omega_- - \mu} \tag{S32}$$

where we leave out $\Gamma_{\pm}^{0}$ since $\Gamma_{\pm}^{0} \ll \Gamma_{-}$ for 7.5 mT $\leq B_{\text{ext}} \leq$11.5 mT (which is the field range corresponding to Fig. 4D of the main text), and $G(T)$ is a function of temperature T. A calculation of Eq. 1 in the main text shows that we can linearize $G(T)$ over the ~40 K temperature change that is relevant in this measurement (Fig. S9E. See section S7 for the determination of the temperature change). Substituting $G(T) = a + b\Delta T$ into Eq. S32, we get

$$\Gamma_{-}(\mu) = \frac{a+b\Delta T}{\hbar\omega_{-}-\mu} = \frac{a+b\Delta T}{\hbar\omega_{-}(1-\frac{\mu}{\hbar\omega_{-}})} \tag{S33}$$

which can be expanded as

$$\Gamma_{-}(\mu) = \frac{a+b\Delta T}{\hbar\omega_{-}}\left(1+\frac{\mu}{\hbar\omega_{-}}\right) = \frac{a}{\hbar\omega_{-}} + \frac{b\Delta T}{\hbar\omega_{-}} + \frac{a\mu}{(\hbar\omega_{-})^{2}} + \frac{b\Delta T\mu}{(\hbar\omega_{-})^{2}} \tag{S34}$$

where we have used $\frac{1}{1-\frac{\mu}{\hbar\omega_{-}}} \approx 1+\frac{\mu}{\hbar\omega_{-}}$ when $\frac{\mu}{\hbar\omega_{-}} \ll 1$.The fourth term of Eq. S34 can be neglected given that $\frac{\mu}{\hbar\omega_{-}} \ll 1$, and $\frac{b\Delta T}{\hbar\omega_{-}} \ll 1$ (Fig. S9E), yielding

$$\Gamma_{-}(\mu) = \Gamma_{-}(0) + \Gamma_{-}(0)\frac{\mu}{\hbar\omega_{-}} + \Gamma_{-}(0)\frac{b\Delta T}{a} \tag{S35}$$

where we have defined $\Gamma_{-}(0) = \frac{a}{\hbar\omega_{-}}$.

We now substitute

$$\mu = A_1 J_{\text{c}} \tag{S36}$$

as expected for the SHE (*14*), where A_1 is a constant, and

$$\Delta T = \beta J_{\text{c}}^{2} \tag{S37}$$

as expected for Ohmic dissipation (and experimentally confirmed in Fig. S9B), with β the fit parameter obtained from Fig. S9B. Substituting Eq. S36 and Eq. S37 into Eq. S35 and defining $A_2 = \frac{b\beta}{a}$, we get

$$\Gamma_{-}(\mu) = \Gamma_{-}(0) + \Gamma_{-}(0)\frac{A_1 J_{\text{c}}}{\hbar\omega_{-}} + \Gamma_{-}(0)A_2 {J_{\text{c}}}^{2} \tag{S38}$$

Finally, by defining $\Gamma_1 = \Gamma_{-}(0)\frac{A_1}{\hbar\omega_{-}}J_{\text{c}}$ and $\Gamma_2 = \Gamma_{-}(0)A_2{J_{\text{c}}}^{2}$, Eq. S38 is reduced to Eq. 5 of the main text. $\Gamma_{-}(0)$, A_1 and A_2 are all obtained from the fit presented in Fig. 4A of the main text.

S9.2 Estimating the chemical potential based on spin transport theory

In this subsection, we compare the measured value of the chemical potential under spin-Hall injection (presented in Fig. 4D of the main text) to an estimate based on spin transport theory.

The spin chemical potential μ_{in} at the Pt side of the Pt/YIG interface can be estimated using Eq. 20 in Ref. 17 (*17*)

$$\mu_{\text{in}} = 2\theta_{\text{SH}} J_{\text{c}} \frac{\lambda_{\text{Pt}}}{\sigma_{\text{Pt}}} \tanh\left(\frac{t_{\text{Pt}}}{2\lambda_{\text{Pt}}}\right)\sin(\phi) \tag{S39}$$

Here, θ_{SH} is the Pt spin-Hall angle, λ_{Pt} is the Pt spin diffusion length, σ_{Pt} is the Pt electrical conductivity, t_{Pt} is the thickness of the Pt stripline, and ϕ is the angle between the magnetization and the Pt stripline. In our experiment (Fig. 4D of the main text), $J_{\text{c}} = 1.2 \times 10^{11}$ A/m^2, $\sigma_{\text{Pt}} = 2 \times 10^{6}$ S/m, t_{Pt} = 10 nm, and ϕ = 52°. It is clear that estimating μ_{in} requires precise knowledge of θ_{SH} and λ_{Pt}. However, the reported values of θ_{SH} vary quite

dramatically from 0.0037 to 0.11, while those of λ_{Pt} range from 1.2 nm to 11 nm (*42-55*). Using these bounds, we estimate that μ_{in} ranges between 0.4 μeV and 49 μeV.

For simplicity, we now assume a perfect Pt/YIG interface (i.e., no decay of chemical potential at the Pt/YIG interface). Furthermore, given the 20-nm YIG thickness, our system is essentially one-dimensional, so that we can expect a simple exponential decay of the chemical potential as a function of the distance r to the edge of the Pt stripline $\mu(r) = \mu_{in} e^{-r/\lambda_{YIG}}$ where λ_{YIG} is the magnon decay length *(17)*. For a 200-nm YIG film, a reported value *(17)* is $\lambda_{YIG} \approx 10$ μm. Considering that magnon relaxation is typically stronger in thinner YIG films, we may expect a smaller λ_{YIG} in our system. We assume $1\ \mu m \leq \lambda_{YIG} \leq 10\ \mu m$ and arrive at an estimated chemical potential ranging from 0.08 μeV to 41 μeV at r =1.7 μm (the site of our NV). We conclude that the measured value of 0.4 μeV (Fig. 4D of the main text) lies within this range. Considering the large range of our estimate, we would like to highlight the unique advantage of our technique, which provides a measurement of the local chemical potential that is independent of unknown device and material properties.

Section S10. Plots of the measured NV relaxation rates and extracted chemical potentials with error bars.

In Figs. 3A, 3B, and 3D of the main text, the error bars were omitted for clarity. In Figs. S11A-C we replot these figures with error bars:

- Figure S11A shows the same data as Fig. 3A of the main text: the NV_1 relaxation rate Γ_- as a function of the on-chip drive power B_{AC}^2 applied at the FMR frequency at three different values of B_{ext} The uncertainties are smaller than ~6% over the entire power and magnetic-field range.
- Figure S11B shows the same data as Fig. 3B of the main text: the chemical potential μ vs FMR drive power B_{AC}^2 for different values of B_{ext}. Based on Eq. 2 of the main text, the uncertainty in μ is given by $\delta\mu = \hbar\omega_{\pm}\left[\frac{\Gamma_{\pm}(0)}{\Gamma_{\pm}(\mu)}\sqrt{\left(\frac{\delta\Gamma_{\pm}(0)}{\Gamma_{\pm}(0)}\right)^2 + \left(\frac{\delta\Gamma_{\pm}(\mu)}{\Gamma_{\pm}(\mu)}\right)^2}\right]$, where we used that the uncertainty in $\omega_{\pm}$ is negligible.
- Figure S11C shows the same data as Fig. 3D of the main text: the low-power region of μ vs FMR drive power B_{AC}^2 for different values of B_{ext}.

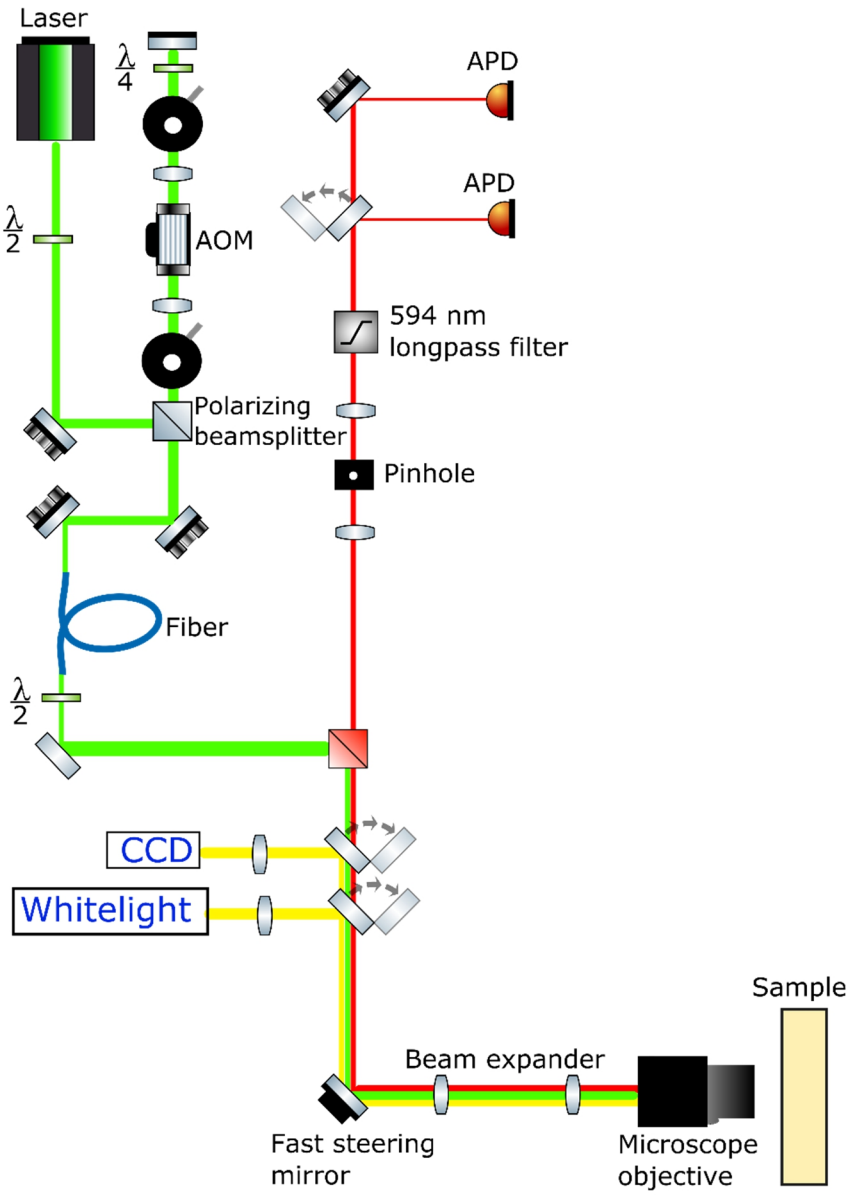


Fig. S1. Home-built scanning confocal microscope setup.
Schematic overview of the confocal setup used in this work. The laser is a Cobolt Samba 532 nm with a power of 100mW. Laser pulses for optical initialization and readout of the NV spin are generated by an acousto-optical modulator (AOM, Isomet 1250C-848) in double-pass configuration. Half- and quarter-waveplates adjust the beam polarization. A single-mode fiber is used as a spatial filter. A fast steering mirror (Newport FSM-300-01) provides 2-axes scanning. The laser is focused onto the sample through a microscopic objective (Olympus MPLFLN50X, NA=0.8). A charge-coupled device (CCD) and a white light source can be used for sample inspection. A dichroic mirror (Semrock FF560-FDi01) reflects the green laser while transmitting the red NV photoluminescence. A longpass filter (Semrock BLP01-594R-25) further suppresses the green laser. Two avalanche photo diodes (APD, Excelitas SPCM-AQRH-13) are used to detect NV photoluminescence and perform photon correlation measurements.

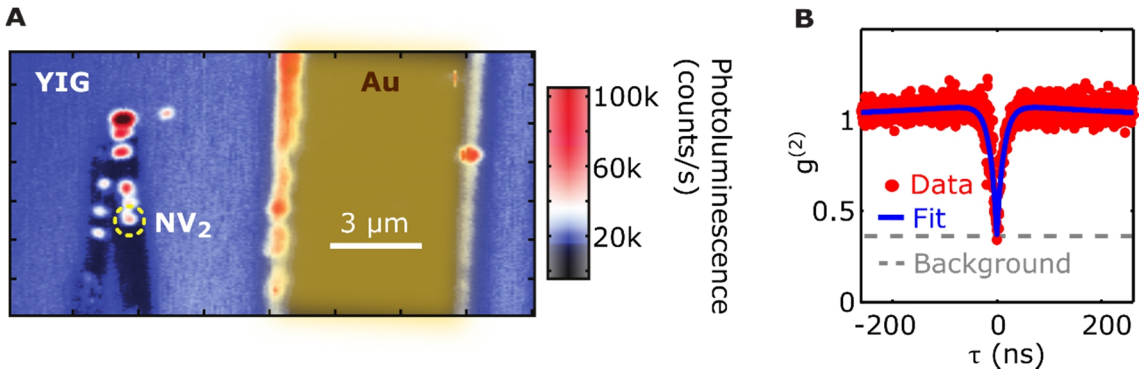


Fig. S2. Addressing single NV centers in diamond nanobeams.
(A) Photoluminescence image showing two diamond nanobeams containing individually addressable NV centers positioned on top of the 20 nm-thick YIG film. The yellow circle indicates the location of the NV_2 center used in this work, which is located at about 4 μm from the Au stripline (false-colored yellow). **(B)** A photon correlation ($g^{(2)}$) measurement on NV_2 indicates a single photon source. Red dots are the measured data and the blue line is a fit based on a three-level model (*34*). The grey dashed line indicates the estimated background contribution. The background is estimated by measuring the photoluminescence of the bare nanobeam at a position next to NV_2.

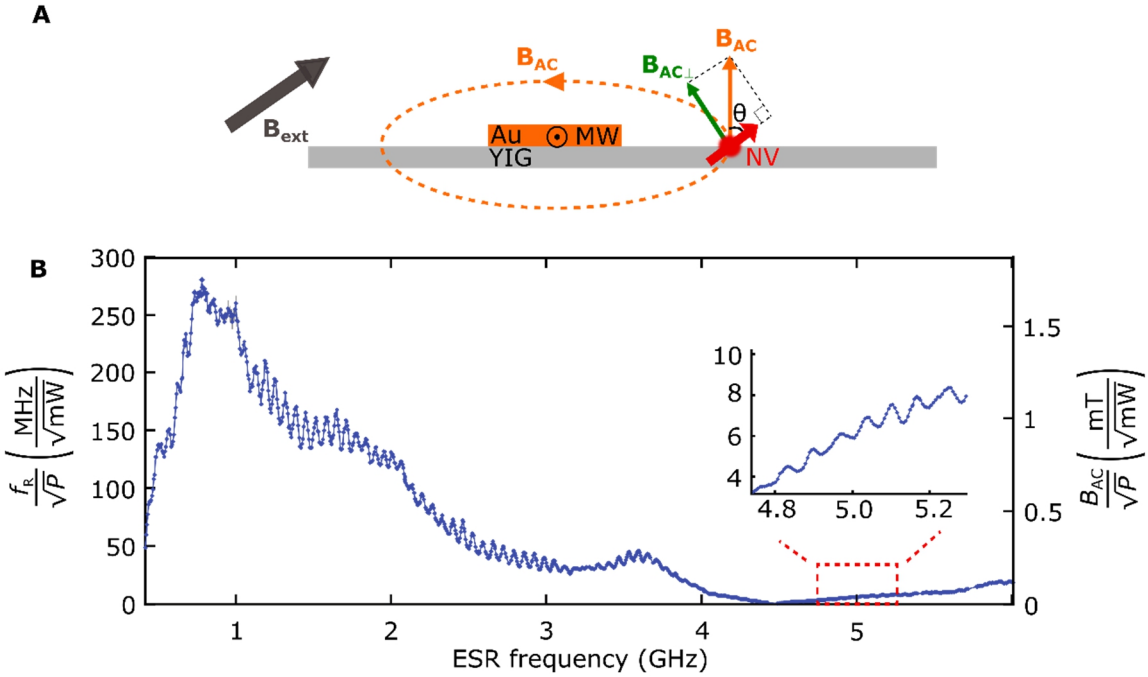


Fig. S3. Calibration of the on-chip AC magnetic field amplitude.
(A) Schematic of the cross-section of the device, showing the direction of the AC magnetic field generated by a MW current in the Au stripline at the NV-site. **(B)** Source-input-power-normalized Rabi frequency as a function of the ESR frequency. This measurement reveals the strongly frequency-dependent MW delivery from the MW source to the chip. P is the MW source power. We use this transmission profile to determine, for a given frequency, the required source power to achieve a desired on-chip AC magnetic field amplitude B_{AC}. Inset: a zoom in of the calibration curve indicating oscillations of microwave transmission with a ~0.07 GHz period.

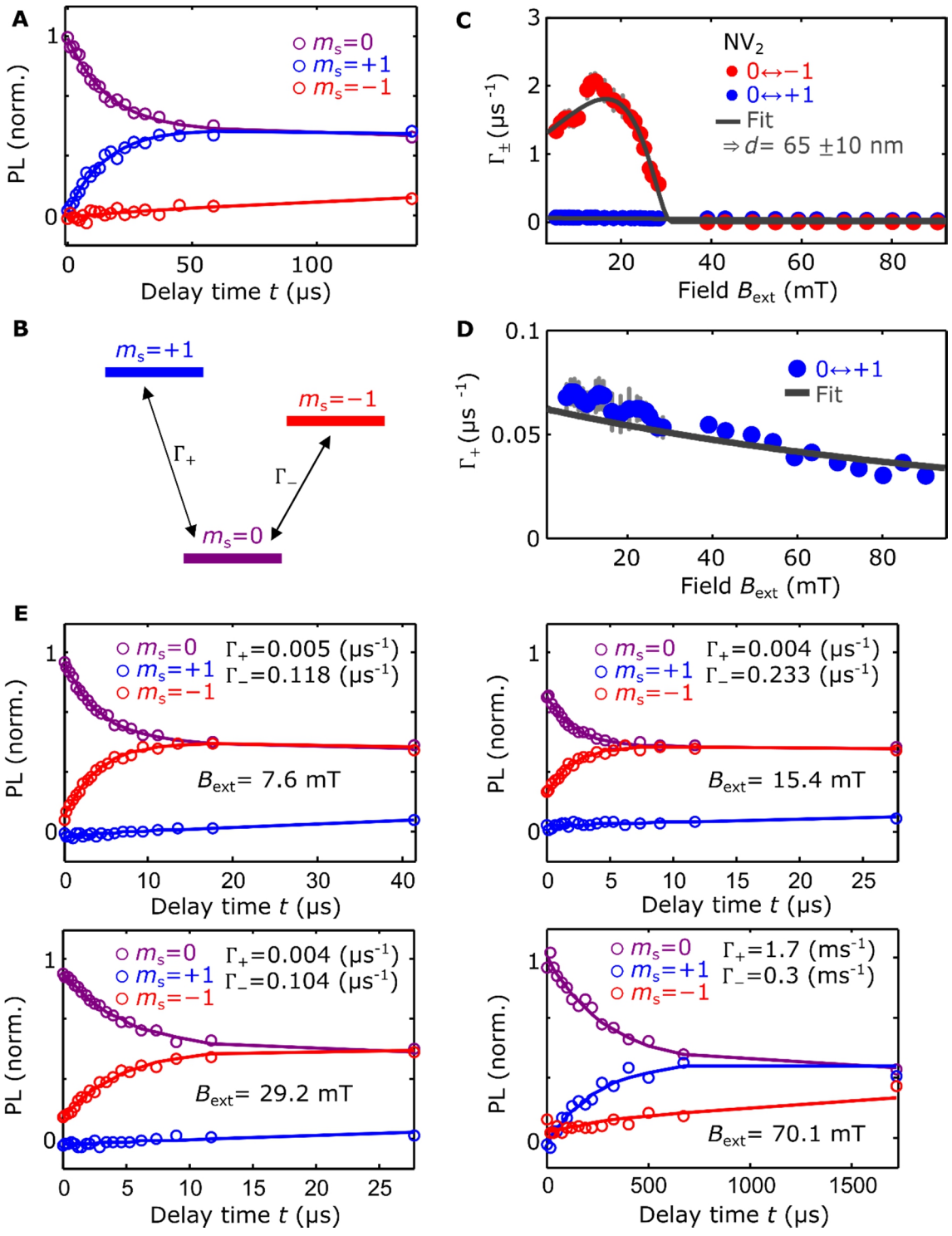


Fig. S4. Measuring the NV spin relaxation rates.
(A) Measurement of the spin relaxation rates of NV_2 at an external field of B_{ext} = 80 mT, performed using the pulse sequence shown in Fig. 2A in the main text. The spin is prepared in the m_s=0 state and let to relax for a time t. At the end of this time, we measure the spin-dependent photoluminescence (PL) either directly ('m_s = 0 readout', purple curve), or after

applying a pi pulse on the $m_s = 0 \leftrightarrow -1$ transition ('m_s = -1 readout', red curve), or after applying a pi pulse on the $m_s = 0 \leftrightarrow +1$ transition ('m_s = +1 readout', blue curve). The relaxation rates $\Gamma_\pm$ are extracted by fitting to a three-level model as described in Section S2. **(B)** Three-level model illustrating the NV relaxation dynamics. **(C)** Spin relaxation rates $\Gamma_\pm$ corresponding to the $m_s = 0 \leftrightarrow \pm 1$ transitions of NV_2 as a function of an external magnetic field, quantifying the magnetic noise emanating from the system. The shape is well described by Eq. 1 of the main text. A fit yields the distance d of NV_2 to the YIG film. **(D)** Zoom-in of (C), showing the spin relaxation rate Γ_+ corresponding to the $m_s = 0 \leftrightarrow +1$ transition of NV_2 as a function of the external magnetic field. Data and fit are the same as in (C). **(E)** Examples of spin-relaxometry measurements from which the relaxation rates $\Gamma_\pm$ shown in Fig. 2A of the main text are extracted, for NV_1 at several different values of B_{ext}.

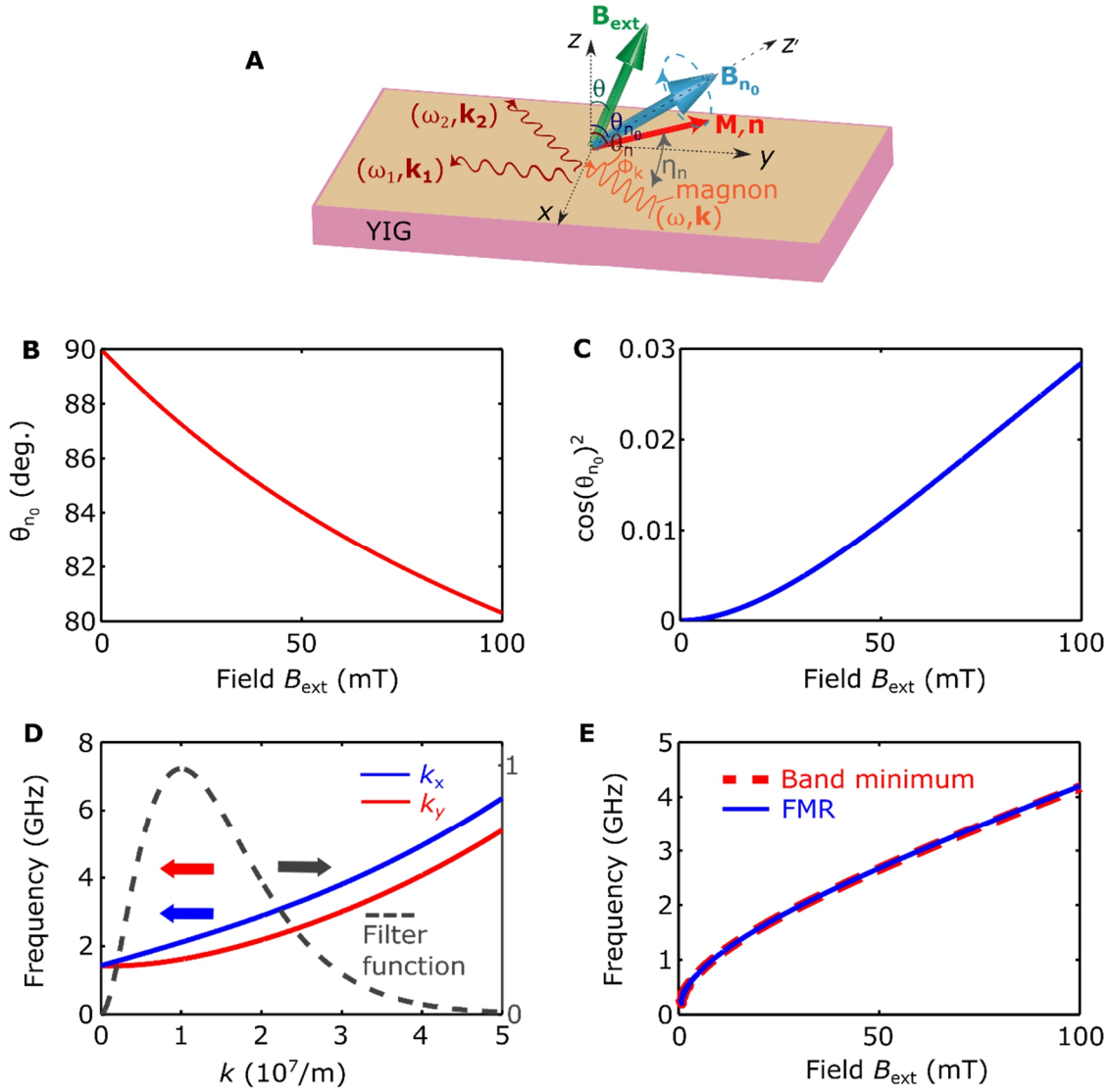


Fig. S5. Coordinate system, magnetization orientation, and magnon dispersion of the 20 nm YIG film.

(A) Coordinate system used for the analyses described in supplementary Section S3, S4 and S5. **(B)** Calculated angle of the internal field θ_{n_0} for a 20 nm YIG film as a function of field B_{ext} at $\theta = 65°$. Note that θ_{n_0} equals the angle of the magnetization. **(C)** Calculated $\cos(\theta_{n_0})^2$ as a function of field B_{ext} at $\theta = 65°$. **(D)** Calculated magnon dispersion (blue and red lines) for a 20 nm YIG film at B_{ext} = 15 mT and $\theta = 65°$. The grey dashed line plots the 'filter function', indicating the range of wavenumbers that can produce a sizable field outside the film and thus be detected by the NV. Note that the FMR itself ($k = 0$) does not generate a magnetic field outside the YIG film. **(E)** Calculated field dependence of the frequency of the magnon band minimum and the FMR, showing that these are essentially at the same frequency, in contrast to micrometer-thick YIG films.

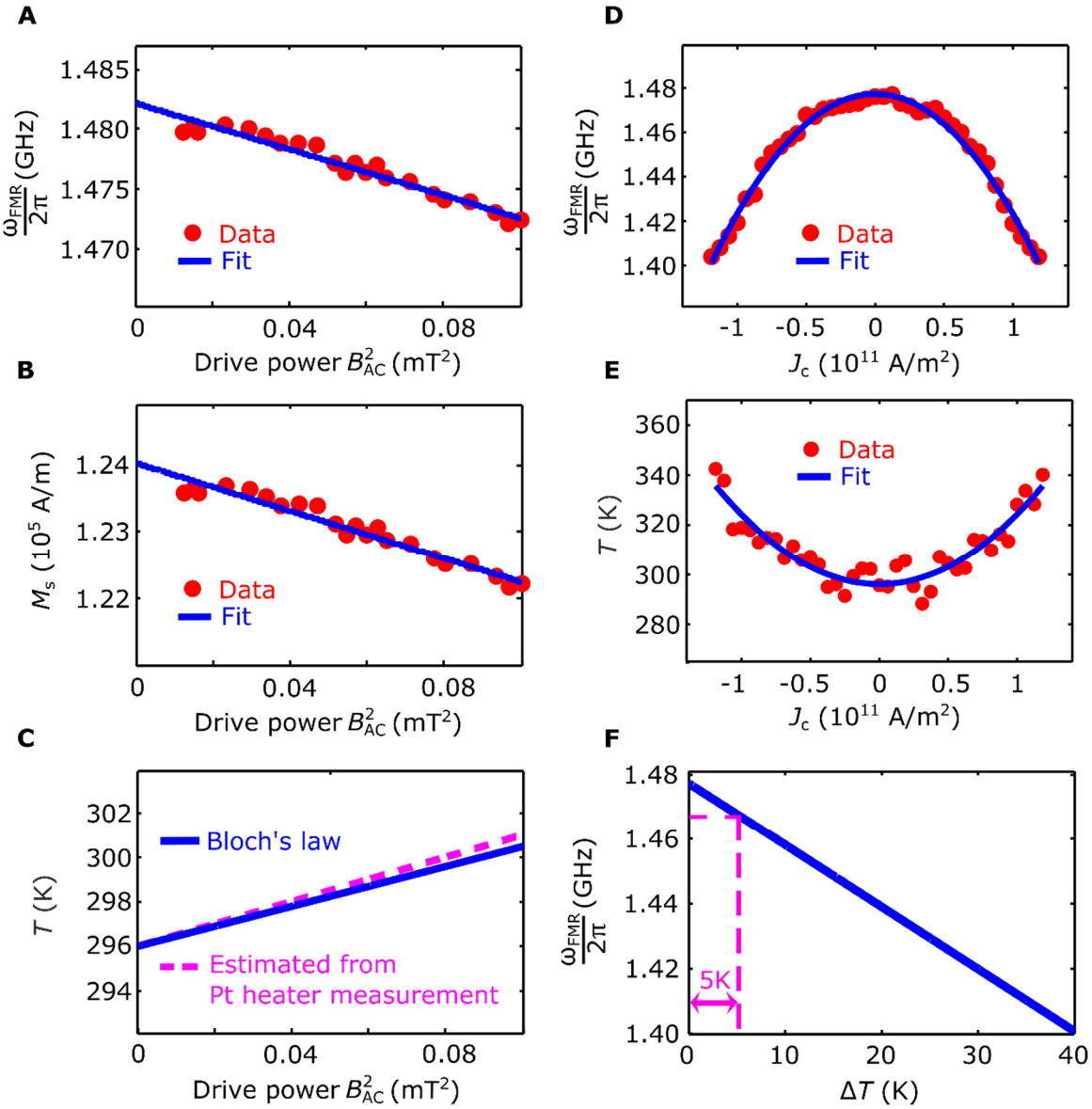


Fig. S6. Estimating the increase in magnon temperature under FMR drive.
(A) FMR frequency ω_{FMR} as a function of FMR drive power B_{AC}^2 at an external magnetic field B_{ext} = 17.4 mT. The red dots are new measurement data. The blue line is a linear fit. **(B)** Change in saturation magnetization M_s as a function of B_{AC}^2, calculated from the data in (A) using Eq. S10. The blue line is a linear fit. **(C)** Upper-bound estimate of the increase in magnon temperature as a function of B_{AC}^2. Blue line: calculated from the data in (B) using Bloch's 3/2 law. Dashed pink line: calculated using an independent calibration measurement of the temperature-induced shift of ω_{FMR} described in (D)-(F). **(D)** FMR frequency as a function of the electrical current density J_c in the Pt wire, measured at B_{ext} = 17.4 mT. Red dots: measurement data. Blue line: quadratic fit. **(E)** Pt-heater-induced temperature change as a function of J_c, obtained by measuring the change in NV zero-field splitting (this is the same figure as Fig. S9B). Red dots: measurement data. Blue line: quadratic fit. **(F)** FMR frequency as a function of Pt-heater-induced temperature change obtained by combining the fits of (D) and (E).

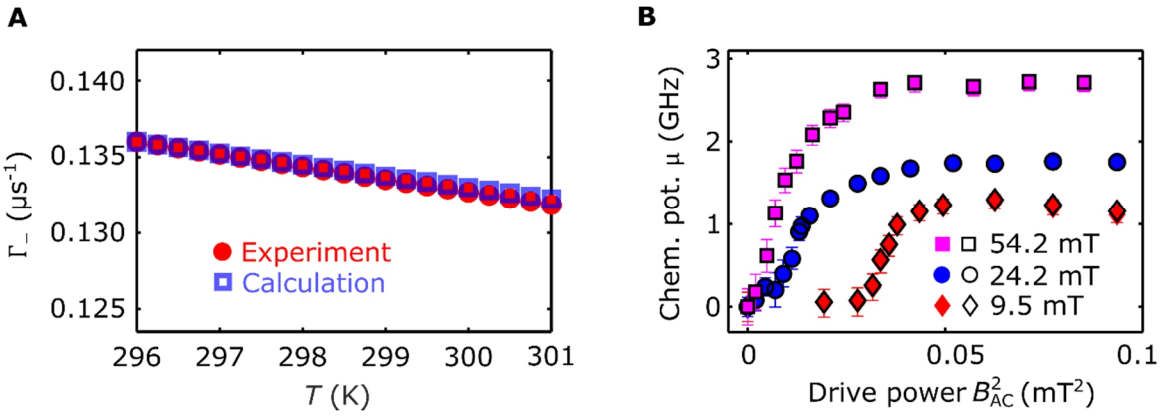


Fig. S7. Including the temperature correction in the chemical potential calculations. **(A)** Red data points: Temperature-induced change in NV relaxation rate, measured using the Pt wire as a local on-chip heater at an external magnetic field of B_{ext} = 9.5 mT. These data are the same as those in Fig. S9E. Blue dots: theoretical calculation of the temperature-induced change based on Eq. 1 of the main text. **(B)** Comparison of the original values of the chemical potential (solid markers, calculated with Eq. 2 of the main text) and the corrected chemical potential values that include the upper-bound estimate of the increase in magnon temperature (empty markers outlined in black, calculated with Eq. S31) at three different values of B_{ext}.

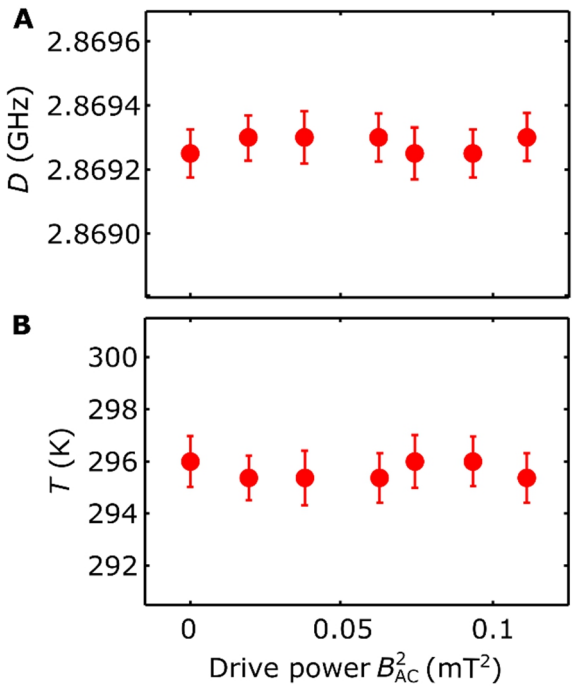


Fig. S8. Analysis of the phonon temperature at the NV site during the application of an FMR drive field.
(A) NV zero field splitting frequency D measured as a function of FMR driving power B_{AC}^2. D is obtained by measuring the NV ESR frequencies and taking the average $D=\frac{\omega_+ + \omega_-}{4\pi}$. **(B)** Temperature as a function of B_{AC}^2 extracted from the results in (A).

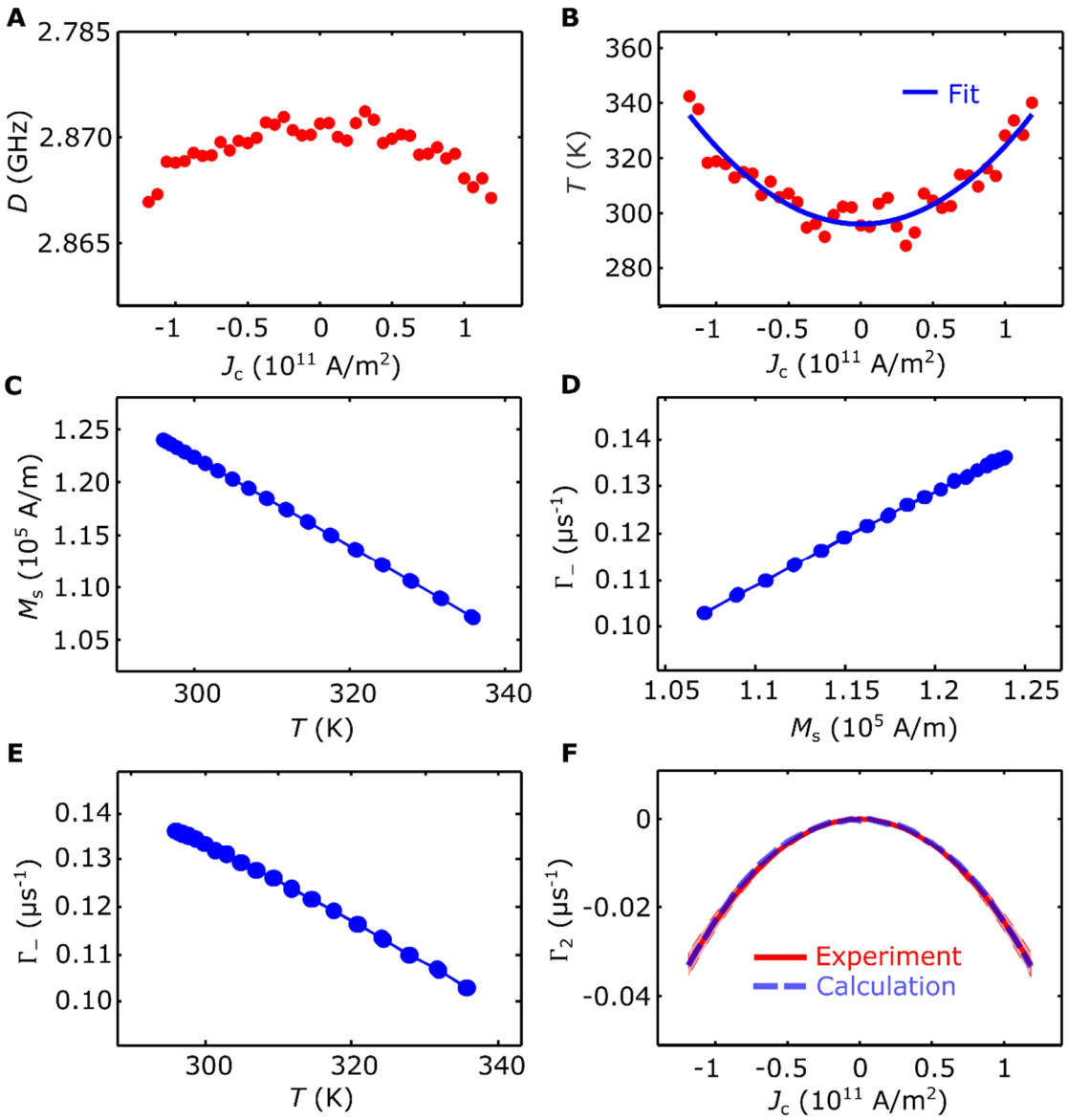


Fig. S9. Effect of heating on the NV spin relaxation rate.
(A) NV zero-field splitting frequency D measured as a function of current density J_c in the Pt stripline. D is determined by measuring the NV ESR frequencies and taking the average $D=\frac{\omega_+ + \omega_-}{4\pi}$. **(B)** Temperature variation as a function of J_c extracted from the results in (A). Red dots are measurement data. The blue line is a quadratic fit. **(C)** Temperature dependence of the YIG saturation magnetization M_s, calculated using a Bloch $T^{3/2}$ law (see text). **(D)**, **(E)**, and **(F)** show the calculated variation of the NV relaxation rate Γ_- as a function of M_s, temperature T, and J_c respectively. The red curve in (F) is the quadratic part of the fit of the measured relaxation rate vs current shown in Fig. 4B of the main text. The red shading indicates a 2 s.d. confidence interval based on the uncertainty of the fit parameter A_2 (see Section S9).

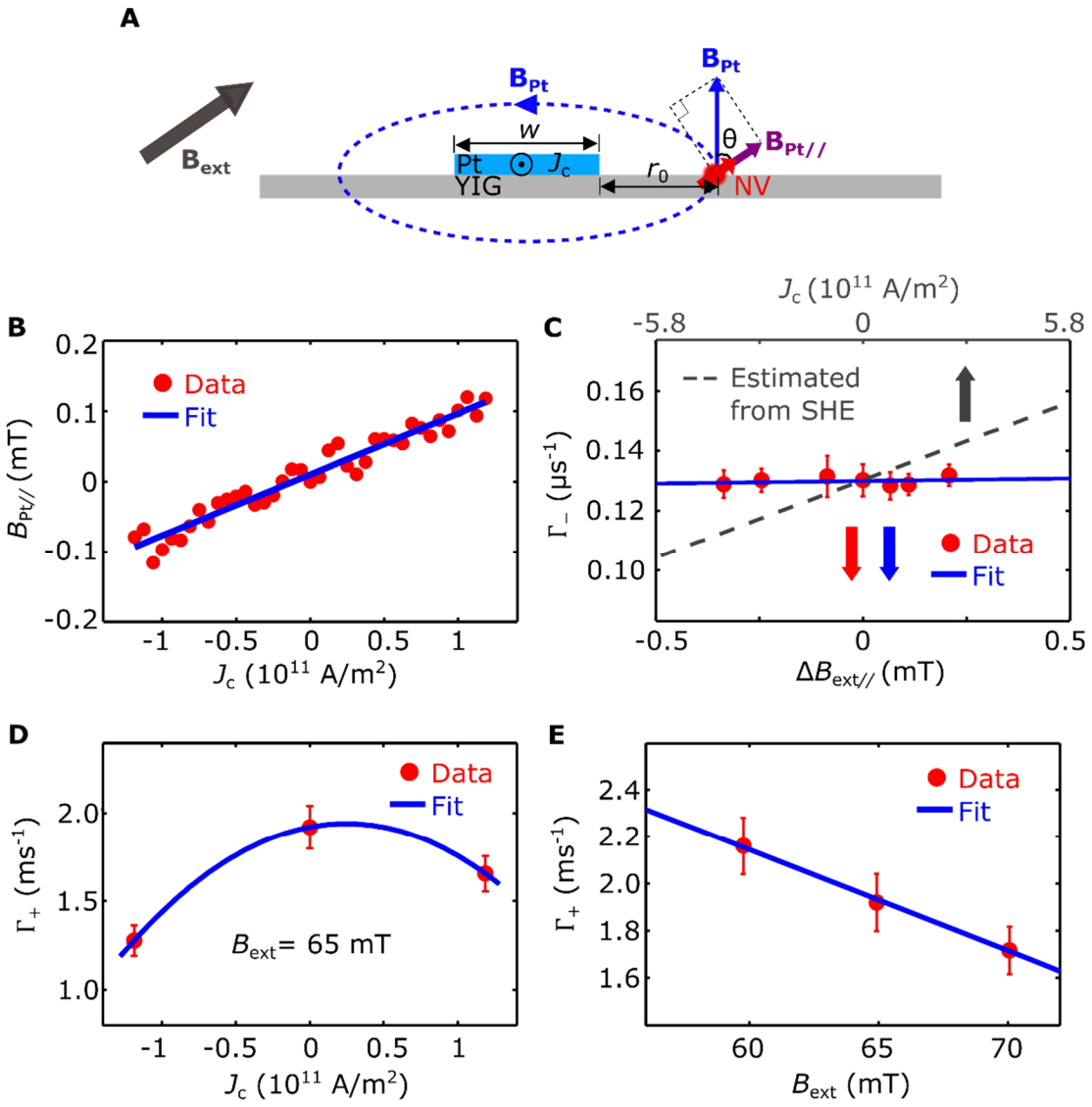


Fig. S10. Effect of the DC field generated by the current in the Pt on the NV relaxation rate.

(A) Schematic cross-section of the device showing the Pt stripline on top of the YIG chip. NV_1 is located at $r_0 \approx 1.7$ µm from the edge of the Pt stripline. An electrical current sent through the Pt generates a DC magnetic field B_{Pt} which is perpendicular to the film plane at the NV location. **(B)** Projection onto the NV axis of the magnetic field generated by the DC current J_c running through the Pt stripline. **(C)** Red dots: control measurement showing the measured NV relaxation rates Γ_- as a function of an externally applied change in magnetic field that mimics the field generated by the Pt stripline, indicating a negligible variation of the rate. The blue line is a linear fit. The grey line is the measured SHE contribution to the change of Γ_- at $B_{ext} = 9.5$ mT **(D)** Current density dependence of the rate Γ_+ at $B_{ext} = 65$ mT. The blue line is a fit based on a second-order polynomial. **(E)** Field dependence of Γ_+ from 60 to 70 mT, measured at zero current through the Pt.

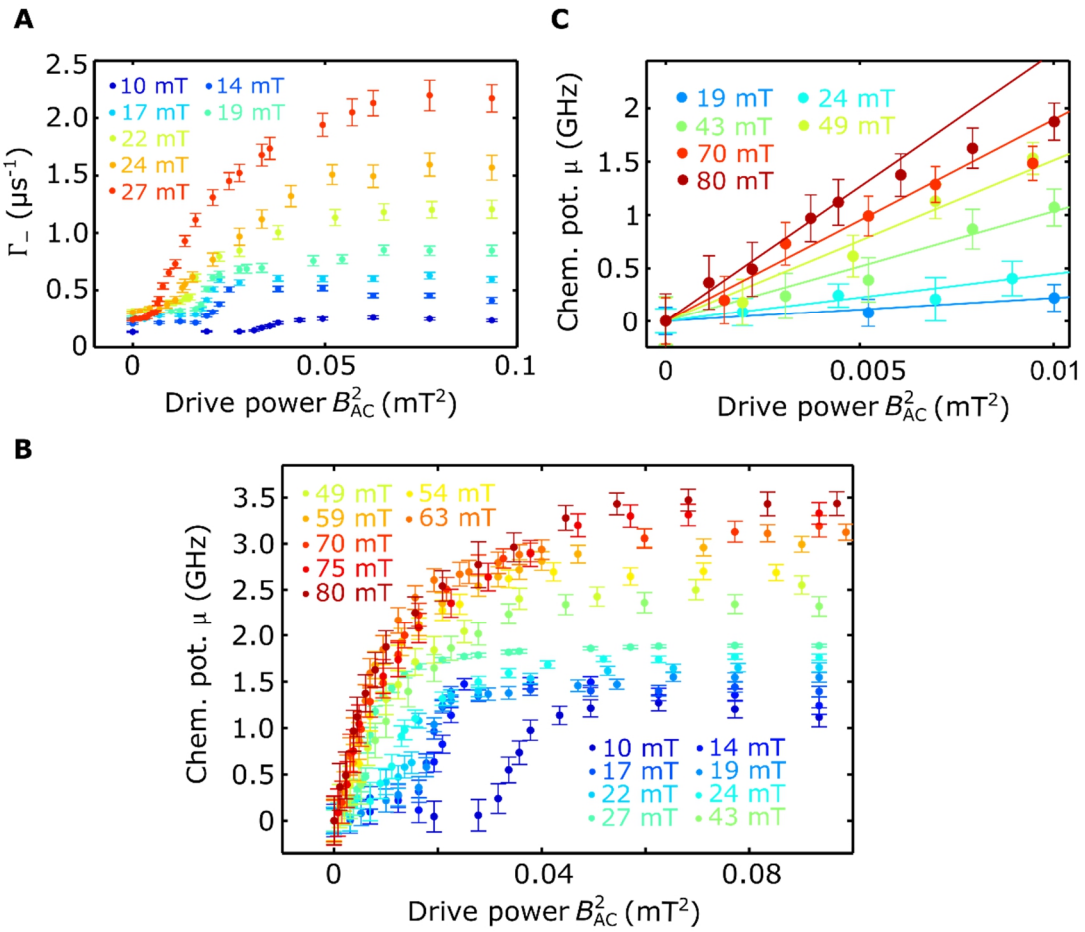


Fig. S11. Same data as in Fig. 3A, 3B, and 3D of the main text, plotted in two dimensions with error bars. (A) NV_1 relaxation rate Γ_- as a function of the on-chip power B_{AC}^2 of a magnetic drive field applied at the FMR frequency at different values of the external magnetic field B_{ext}. **(B)** Chemical potential μ as a function of B_{AC}^2 at different values of B_{ext}. **(C)** In the low drive power region, the chemical potential μ increases linearly at a rate $d\mu/dB_{AC}^2$ that depends on B_{ext}. In all plots, the values of B_{ext} are indicated in the legends.

References and Notes

1. M. W. Zwierlein, A. Schirotzek, C. H. Schunck, W. Ketterle, Fermionic superfluidity with imbalanced spin populations. *Science* **311**, 492–496 (2006). doi:10.1126/science.1122318 Medline

2. S. Sachdev, *Quantum Phase Transitions* (Cambridge Univ. Press, ed. 2, 2011).

3. S. O. Demokritov, V. E. Demidov, O. Dzyapko, G. A. Melkov, A. A. Serga, B. Hillebrands, A. N. Slavin, Bose-Einstein condensation of quasi-equilibrium magnons at room temperature under pumping. *Nature* **443**, 430–433 (2006). doi:10.1038/nature05117 Medline

4. S. A. Bender, R. A. Duine, Y. Tserkovnyak, Electronic pumping of quasiequilibrium Bose-Einstein-condensed magnons. *Phys. Rev. Lett.* **108**, 246601 (2012). doi:10.1103/PhysRevLett.108.246601 Medline

5. A. Sommer, M. Ku, G. Roati, M. W. Zwierlein, Universal spin transport in a strongly interacting Fermi gas. *Nature* **472**, 201–204 (2011). doi:10.1038/nature09989 Medline

6. F. J. Jedema, A. T. Filip, B. J. van Wees, Electrical spin injection and accumulation at room temperature in an all-metal mesoscopic spin valve. *Nature* **410**, 345–348 (2001). doi:10.1038/35066533 Medline

7. B. Dlubak, M.-B. Martin, C. Deranlot, B. Servet, S. Xavier, R. Mattana, M. Sprinkle, C. Berger, W. A. De Heer, F. Petroff, A. Anane, P. Seneor, A. Fert, Highly efficient spin transport in epitaxial graphene on SiC. *Nat. Phys.* **8**, 557–561 (2012). doi:10.1038/nphys2331

8. Y. Fukuma, L. Wang, H. Idzuchi, S. Takahashi, S. Maekawa, Y. Otani, Giant enhancement of spin accumulation and long-distance spin precession in metallic lateral spin valves. *Nat. Mater.* **10**, 527–531 (2011). doi:10.1038/nmat3046 Medline

9. B. Flebus, S. A. Bender, Y. Tserkovnyak, R. A. Duine, Two-fluid theory for spin superfluidity in magnetic insulators. *Phys. Rev. Lett.* **116**, 117201 (2016). doi:10.1103/PhysRevLett.116.117201 Medline

10. C. M. Jaworski, J. Yang, S. Mack, D. D. Awschalom, J. P. Heremans, R. C. Myers, Observation of the spin-Seebeck effect in a ferromagnetic semiconductor. *Nat. Mater.* **9**, 898–903 (2010). doi:10.1038/nmat2860 Medline

11. G. E. W. Bauer, E. Saitoh, B. J. van Wees, Spin caloritronics. *Nat. Mater.* **11**, 391–399 (2012). doi:10.1038/nmat3301 Medline

12. A. V. Chumak, V. I. Vasyuchka, A. A. Serga, B. Hillebrands, Magnon spintronics. *Nat. Phys.* **11**, 453–461 (2015). doi:10.1038/nphys3347

13. I. Žutić, J. Fabian, S. Das Sarma, Spintronics: Fundamentals and applications. *Rev. Mod. Phys.* **76**, 323–410 (2004). doi:10.1103/RevModPhys.76.323

14. L. J. Cornelissen, J. Liu, R. A. Duine, J. B. Youssef, B. J. van Wees, Long distance transport of magnon spin information in a magnetic insulator at room temperature. *Nat. Phys.* **11**, 1022–1026 (2015). doi:10.1038/nphys3465

15. J. Sinova, S. O. Valenzuela, J. Wunderlich, C. H. Back, T. Jungwirth, Spin Hall effects. *Rev.*

Mod. Phys. **87**, 1213–1260 (2015). doi:10.1103/RevModPhys.87.1213

16. J. Bass, W. P. Pratt Jr., Spin-diffusion lengths in metals and alloys, and spin-flipping at metal/metal interfaces: An experimentalist's critical review. *J. Phys. Condens. Matter* **19**, 183201 (2007). doi:10.1088/0953-8984/19/18/183201

17. L. J. Cornelissen, K. J. H. Peters, G. E. W. Bauer, R. A. Duine, B. J. van Wees, Magnon spin transport driven by the magnon chemical potential in a magnetic insulator. *Phys. Rev. B* **94**, 014412 (2016). doi:10.1103/PhysRevB.94.014412

18. S. O. Demokritov, V. E. Demidov, Micro-brillouin light scattering spectroscopy of magnetic nanostructures. *IEEE Trans. Magn.* **44**, 6–12 (2008). doi:10.1109/TMAG.2007.910227

19. J. R. Maze, P. L. Stanwix, J. S. Hodges, S. Hong, J. M. Taylor, P. Cappellaro, L. Jiang, M. V. G. Dutt, E. Togan, A. S. Zibrov, A. Yacoby, R. L. Walsworth, M. D. Lukin, Nanoscale magnetic sensing with an individual electronic spin in diamond. *Nature* **455**, 644–647 (2008). doi:10.1038/nature07279 Medline

20. L. Rondin, J.-P. Tetienne, T. Hingant, J.-F. Roch, P. Maletinsky, V. Jacques, Magnetometry with nitrogen-vacancy defects in diamond. *Rep. Prog. Phys.* **77**, 056503 (2014). doi:10.1088/0034-4885/77/5/056503 Medline

21. M. J. Burek, N. P. de Leon, B. J. Shields, B. J. M. Hausmann, Y. Chu, Q. Quan, A. S. Zibrov, H. Park, M. D. Lukin, M. Lončar, Free-standing mechanical and photonic nanostructures in single-crystal diamond. *Nano Lett.* **12**, 6084–6089 (2012). doi:10.1021/nl302541e Medline

22. A. Gruber, A. Dräbenstedt, C. Tietz, L. Fleury, J. Wrachtrup, C. von Borczyskowski, Scanning confocal optical microscopy and magnetic resonance on single defect centers. *Science* **276**, 2012–2014 (1997). doi:10.1126/science.276.5321.2012

23. Materials and methods are available as supplementary materials.

24. T. van der Sar, F. Casola, R. Walsworth, A. Yacoby, Nanometre-scale probing of spin waves using single-electron spins. *Nat. Commun.* **6**, 7886 (2015). doi:10.1038/ncomms8886 Medline

25. C. S. Wolfe, V. P. Bhallamudi, H. L. Wang, C. H. Du, S. Manuilov, R. M. Teeling-Smith, A. J. Berger, R. Adur, F. Y. Yang, P. C. Hammel, Off-resonant manipulation of spins in diamond via precessing magnetization of a proximal ferromagnet. *Phys. Rev. B* **89**, 180406 (2014). doi:10.1103/PhysRevB.89.180406

26. M. R. Page, F. Guo, C. M. Purser, J. G. Schulze, T. M. Nakatani, C. S. Wolfe, J. R. Childress, P. C. Hammel, G. D. Fuchs, V. P. Bhallamudi, Optically detected ferromagnetic resonance in metallic ferromagnets via nitrogen vacancy centers in diamond. arXiv:1607.07485 [cond-mat.mes-hall](2016).

27. S. A. Bender, Y. Tserkovnyak, Thermally driven spin torques in layered magnetic insulators. *Phys. Rev. B* **93**, 064418 (2016). doi:10.1103/PhysRevB.93.064418

28. M. C. Onbasli, A. Kehlberger, D. H. Kim, G. Jakob, M. Kläui, A. V. Chumak, B. Hillebrands, C. A. Ross, Pulsed laser deposition of epitaxial yttrium iron garnet films with low Gilbert damping and bulk-like magnetization. *APL Mater.* **2**, 106102 (2014). doi:10.1063/1.4896936

29. B. Flebus, P. Upadhyaya, R. A. Duine, Y. Tserkovnyak, Local thermomagnonic torques in two-fluid spin dynamics. *Phys. Rev. B* **94**, 214428 (2016). doi:10.1103/PhysRevB.94.214428

30. M. Collet, X. de Milly, O. d'Allivy Kelly, V. V. Naletov, R. Bernard, P. Bortolotti, J. Ben Youssef, V. E. Demidov, S. O. Demokritov, J. L. Prieto, M. Muñoz, V. Cros, A. Anane, G. de Loubens, O. Klein, Generation of coherent spin-wave modes in yttrium iron garnet microdiscs by spin-orbit torque. *Nat. Commun.* **7**, 10377 (2016). doi:10.1038/ncomms10377 Medline

31. L. Liu, C.-F. Pai, Y. Li, H. W. Tseng, D. C. Ralph, R. A. Buhrman, Spin-torque switching with the giant spin Hall effect of tantalum. *Science* **336**, 555–558 (2012). doi:10.1126/science.1218197 Medline

32. V. M. Acosta, E. Bauch, M. P. Ledbetter, A. Waxman, L.-S. Bouchard, D. Budker, Temperature dependence of the nitrogen-vacancy magnetic resonance in diamond. *Phys. Rev. Lett.* **104**, 070801 (2010). doi:10.1103/PhysRevLett.104.070801 Medline

33. S. A. Manuilov, R. Fors, S. I. Khartsev, A. M. Grishin, Submicron $Y_3Fe_5O_{12}$ film magnetostatic wave band pass filters. *J. Appl. Phys.* **105**, 033917 (2009). doi:10.1063/1.3075816

34. C. Kurtsiefer, S. Mayer, P. Zarda, H. Weinfurter, Stable solid-state source of single photons. *Phys. Rev. Lett.* **85**, 290–293 (2000). doi:10.1103/PhysRevLett.85.290 Medline

35. R. Hanson, V. V. Dobrovitski, A. E. Feiguin, O. Gywat, D. D. Awschalom, Coherent dynamics of a single spin interacting with an adjustable spin bath. *Science* **320**, 352–355 (2008). doi:10.1126/science.1155400 Medline

36. T. H. Taminiau, J. Cramer, T. van der Sar, V. V. Dobrovitski, R. Hanson, Universal control and error correction in multi-qubit spin registers in diamond. *Nat. Nanotechnol.* **9**, 171–176 (2014). doi:10.1038/nnano.2014.2 Medline

37. A. G. Gurevich, G. A. Melkov, *Magnetization Oscillations and Waves* (CRC Press, 1996).

38. B. A. Kalinikos, A. N. Slavin, Theory of dipole-exchange spin wave spectrum for ferromagnetic films with mixed exchange boundary conditions. *J. Phys. C Solid State Phys.* **19**, 7013–7033 (1986). doi:10.1088/0022-3719/19/35/014

39. M. Lundstrom, *Fundamentals of Carrier Transport* (Cambridge Univ. Press, 2000), vol. 13.

40. L. D. Landau, E. M. Lifshitz, *Statistical Physics, Part 1* (Elsevier, 1980), vol. 5.

41. P. Neumann, I. Jakobi, F. Dolde, C. Burk, R. Reuter, G. Waldherr, J. Honert, T. Wolf, A. Brunner, J. H. Shim, D. Suter, H. Sumiya, J. Isoya, J. Wrachtrup, High-precision nanoscale temperature sensing using single defects in diamond. *Nano Lett.* **13**, 2738–2742 (2013). doi:10.1021/nl401216y Medline

42. T. Kimura, Y. Otani, T. Sato, S. Takahashi, S. Maekawa, Room-temperature reversible spin Hall effect. *Phys. Rev. Lett.* **98**, 156601 (2007). doi:10.1103/PhysRevLett.98.156601 Medline

43. L. Vila, T. Kimura, Y. Otani, Evolution of the spin Hall effect in Pt nanowires: Size and temperature effects. *Phys. Rev. Lett.* **99**, 226604 (2007).

doi:10.1103/PhysRevLett.99.226604 Medline

44. O. Mosendz, V. Vlaminck, J. E. Pearson, F. Y. Fradin, G. E. W. Bauer, S. D. Bader, A. Hoffmann, Detection and quantification of inverse spin Hall effect from spin pumping in permalloy/normal metal bilayers. *Phys. Rev. B* **82**, 214403 (2010). doi:10.1103/PhysRevB.82.214403

45. O. Mosendz, J. E. Pearson, F. Y. Fradin, G. E. W. Bauer, S. D. Bader, A. Hoffmann, Quantifying spin Hall angles from spin pumping: Experiments and theory. *Phys. Rev. Lett.* **104**, 046601 (2010). doi:10.1103/PhysRevLett.104.046601 Medline

46. A. Azevedo, L. H. Vilela-Leão, R. L. Rodríguez-Suárez, A. F. Lacerda Santos, S. M. Rezende, Spin pumping and anisotropic magnetoresistance voltages in magnetic bilayers: Theory and experiment. *Phys. Rev. B* **83**, 144402 (2011). doi:10.1103/PhysRevB.83.144402

47. K. Ando, S. Takahashi, J. Ieda, Y. Kajiwara, H. Nakayama, T. Yoshino, K. Harii, Y. Fujikawa, M. Matsuo, S. Maekawa, E. Saitoh, Inverse spin-Hall effect induced by spin pumping in metallic system. *J. Appl. Phys.* **109**, 103913 (2011). doi:10.1063/1.3587173

48. L. Liu, T. Moriyama, D. C. Ralph, R. A. Buhrman, Spin-torque ferromagnetic resonance induced by the spin Hall effect. *Phys. Rev. Lett.* **106**, 036601 (2011). doi:10.1103/PhysRevLett.106.036601 Medline

49. M. Morota, Y. Niimi, K. Ohnishi, D. H. Wei, T. Tanaka, H. Kontani, T. Kimura, Y. Otani, Indication of intrinsic spin Hall effect in 4d and 5d transition metals. *Phys. Rev. B* **83**, 174405 (2011). doi:10.1103/PhysRevB.83.174405

50. Z. Feng, J. Hu, L. Sun, B. You, D. Wu, J. Du, W. Zhang, A. Hu, Y. Yang, D. M. Tang, B. S. Zhang, H. F. Ding, Spin Hall angle quantification from spin pumping and microwave photoresistance. *Phys. Rev. B* **85**, 214423 (2012). doi:10.1103/PhysRevB.85.214423

51. M. Althammer, S. Meyer, H. Nakayama, M. Schreier, S. Altmannshofer, M. Weiler, H. Huebl, S. Geprägs, M. Opel, R. Gross, D. Meier, C. Klewe, T. Kuschel, J.-M. Schmalhorst, G. Reiss, L. Shen, A. Gupta, Y.-T. Chen, G. E. W. Bauer, E. Saitoh, S. T. B. Goennenwein, Quantitative study of the spin Hall magnetoresistance in ferromagnetic insulator/normal metal hybrids. *Phys. Rev. B* **87**, 224401 (2013). doi:10.1103/PhysRevB.87.224401

52. M. Weiler, M. Althammer, M. Schreier, J. Lotze, M. Pernpeintner, S. Meyer, H. Huebl, R. Gross, A. Kamra, J. Xiao, Y. T. Chen, H. Jiao, G. E. W. Bauer, S. T. B. Goennenwein, Experimental test of the spin mixing interface conductivity concept. *Phys. Rev. Lett.* **111**, 176601 (2013). doi:10.1103/PhysRevLett.111.176601 Medline

53. W. Zhang, V. Vlaminck, J. E. Pearson, R. Divan, S. D. Bader, A. Hoffmann, Determination of the Pt spin diffusion length by spin-pumping and spin Hall effect. *Appl. Phys. Lett.* **103**, 242414 (2013). doi:10.1063/1.4848102

54. H. L. Wang, C. H. Du, Y. Pu, R. Adur, P. C. Hammel, F. Y. Yang, Scaling of spin Hall angle in 3d, 4d, and 5d metals from $Y_3Fe_5O_{12}$/metal spin pumping. *Phys. Rev. Lett.* **112**, 197201 (2014). doi:10.1103/PhysRevLett.112.197201 Medline

55. D. Qu, S. Y. Huang, B. F. Miao, S. X. Huang, C. L. Chien, Self-consistent determination of

spin Hall angles in selected 5d metals by thermal spin injection. *Phys. Rev. B* **89**, 140407 (2014). doi:10.1103/PhysRevB.89.140407